



Control Blade Insertion Dynamics in Pebble-Bed Fluoride-Salt-Cooled High-Temperature Reactors

Grant Buster
Ryan Sawadichai
Michael Laufer
Per Peterson

UCBTH-15-005

May 21, 2015
Department of Nuclear Engineering
University of California, Berkeley

This research is being performed using funding received from the U.S. Department of Energy Office of Nuclear Energy's Nuclear Energy University Programs.

This document is for distribution.



Contents

List of Figures	3
List of Tables	6
Acronyms and Abbreviations	7
1 Introduction to the Control Blade Insertion Experiment (CoBIE)	8
2 Experimental Setup	10
2.1 CoBIE Physical Description	10
2.2 Notes on CoBIE Scaling	14
2.3 Controls and Sensors	18
2.4 Experimental Procedure	20
2.4.1 Insertion Force Test Procedure.....	20
2.4.2 Pebble Tomography Experimental Test Procedure	21
2.5 Test Matrix	22
3 Data Analysis Techniques	24
3.1 Insertion Force Profiles	24
3.1.1 Maximum Insertion Force and Uncertainty Analysis.....	24
3.1.2 Treatment of Insertion Forces Using the Weibull Distribution Function	25
3.2 X-PETS Data and CoBIE Custom Post Processing Module	30
4 CoBIE Experimental Results	33
4.1 Blade Insertion Hysteresis and Resistance Modes to Blade Insertion	33
4.1.1 Insertion Force Hysteresis	33
4.1.2 Pebble Location Hysteresis.....	34
4.1.3 Blade Tip Jamming vs. Drag Force	37
4.2 The Effect of a Bullnose Tip on Blade Insertion	37
4.3 Effects of Blade Angle and Tip Design	38
5 Discussion of CoBIE Results	43
5.1 Analysis of Potential Pebble Failure Caused By Control Blade Insertion	43
5.2 Control Blade Buckling and Deflection Considerations	44
5.2.1 Blade Loading in the Axial Direction.....	44
5.2.2 Blade Deflection Due to Lateral Forces	47
5.3 Scaling Distortions Analysis	48
5.3.1 Effects of the CoBIE Test Silo Constraints	48
5.3.2 Velocity Distortions.....	50
5.3.3 Effects of Lubricity, Coefficient of Restitution and Coolant Flow	52
6 Conclusions and Recommendations for Future Work	54
References	55

List of Figures

Figure 1-1. THTR core with control elements inserted [4] (left) and Mk1 PB-FHR core internals render [1] (right).	9
Figure 2-1. CoBIE test silo physical arrangement without a packed pebble bed. Left: acrylic test silo with 45-degree wedge insert, control blade, and instrumented pebbles. Right: acrylic test silo mounted on the X-PREX assembly with linear actuator retracted and x-ray detector in-view.	11
Figure 2-2. Detailed view of the modular inserts that feature Teflon sleeves for low friction blade insertion. Left: the 45-degree wedge. Right: the 0-degree wedge.	12
Figure 2-3. Primary control blade design. Left: cruciform cross section (dimensions in centimeters). Right: Actual blade compared to the 1.257 cm diameter pebbles. ...	12
Figure 2-4. Two blade geometries with annotations showing the unconstrained angles in the tip. Left: 30-degree two-angle blade. Right: 30-degree three-angle blade.	13
Figure 2-5. 5-angle blade tip with a pebble diameter shown as a circle for scale.	13
Figure 2-6. Three blade tips with a full bullnose (left), half bullnose (middle) and no bullnose (right).	14
Figure 2-7. Wiring schematic for the force sensors. Voltage probe is representative of the DAQ-6009.	18
Figure 2-8. 17-point calibration of three Tekscan FlexiForce A401 Sensors with resulting fit function. Error bars show one standard deviation (326 pebble masses).	19
Figure 2-9. Detailed view of force sensor setup during an experiment.	19
Figure 2-10. Five-point calibration of two Tekscan FlexiForce A401 Sensors for retraction force tests. Linear fit is shown with one-sigma error bars (90 pebble masses).	20
Figure 2-11. Sheath of instrumented pebbles (white) surrounded by non-instrumented pebbles (green) for a localized tomography study. Left image shows cardboard divider used to segregate pebble regions. Right image shows bed after the divider is removed.	22
Figure 3-1. Typical insertion force profiles with average maximum force and one-sigma uncertainties calculated from five peak forces. Sensor uncertainty is included in the standard deviations. Tests performed with the 45-degree wedge, pebble bed height of 48d, and the 45-degree two-angle full-bullnose blade.	24
Figure 3-2. Maximum force methodology for five identical experiments. Insertion velocities= 0.803 ± 0.014 d/s. All tests performed with the 45-degree wedge, pebble bed height of 48d, and the 45-degree two-angle full-bullnose blade.	25
Figure 3-3. Force profile data subset selection for Weibull statistics. Tests performed with the 45-degree wedge, pebble bed height of 48d, and the 45-degree two-angle full-bullnose blade.	26
Figure 3-4. Weibull correlations for five identical blade insertion experiments. Insertion velocities= 0.803 ± 0.014 d/s. All tests performed with the 45-degree wedge, pebble bed height of 48d, and the 45-degree two-angle full-bullnose blade.	27
Figure 3-5. Weibull probability density function (left) and cumulative distribution function (right). Test performed with the 45-degree wedge, pebble bed height of 48d, and the 45-degree two-angle full-bullnose blade.	28

Figure 3-6. Five Weibull PDFs for five identical blade insertion experiments. Insertion velocities= 0.803 ± 0.014 d/s. All tests performed with the 45-degree wedge, pebble bed height of $48d$, and the 45-degree two-angle full-bullnose blade.	29
Figure 3-7. Five Weibull CDFs for five identical blade insertion experiments. Insertion velocities= 0.803 ± 0.014 d/s. All tests performed with the 45-degree wedge, pebble bed height of $48d$, and the 45-degree two-angle full-bullnose blade.	29
Figure 3-8. Left: x-ray image showing the XZ the plane corresponding to Figure 3-9. Instrumented pebbles can be seen by the tungsten wire running through their centers. In this image, gravity points downward and the blade is inserted upward. Right: corresponding blade orientation and pebble for scale.	31
Figure 3-9. Pebble tomography results corresponding to Figure 3-8, showing the XZ plane (gravity points in the $-z$ direction and the blade is inserted in the $+z$ direction $0.98d$). Pebbles are rendered in their final position with varying color and transparency correlated to their normalized centroid displacement from their initial position before the blade was moved. The superimposed white line shows the approximate leading-edge of the final blade position. Pebble centroid displacements are normalized by the blade displacement. Note: $z/d=0$ in this plot does not correspond to $z/d=0$ in the insertion force profile plots.	32
Figure 4-1. Insertion and retraction force hysteresis for five insertions/retractions without intermediate bed mixing. Tests performed using the 45 degree wedge, a pebble bed height of $48d$, and the 45 degree two-angle no-bullnose blade.	33
Figure 4-2. Maximum insertion and retraction forces for five subsequent blade insertion/retraction force tests without intermediate bed mixing. Tests performed using the 45-degree wedge, a pebble bed height of $48d$, and the 45-degree two-angle no-bullnose blade.	34
Figure 4-3. X-ray images showing the YZ plane with red '+'s indicating the centroids of the instrumented pebbles. Gravity points in the $-z$ direction (towards the bottom of the image) and the blade is inserted in the $+z$ direction (towards the top of the image). Left: randomly ordered bed before blade insertion. Middle: bed shown with blade fully inserted. Right: the same bed after full blade insertion and subsequent retraction.	35
Figure 4-4. Histogram showing the number of pebbles as a function of their centroid y-position before blade insertion (the left image in Figure 4-3). $y/d=0$ corresponds to the center of the blade in the images in Figure 4-3.	36
Figure 4-5. Histogram showing the number of pebbles as a function of their centroid y-position while blade is inserted (the middle image in Figure 4-3). $y/d=0$ corresponds to the center of the blade in the images in Figure 4-3.	36
Figure 4-6. Histogram showing the number of pebbles as a function of their centroid y-position after blade retraction (the right image in Figure 4-3). $y/d=0$ corresponds to the center of the blade in the images in Figure 4-3.	37
Figure 4-7. Maximum insertion forces +/- one standard deviation vs. blade insertion position for three blades. Test performed with the 45° wedge insert and the 45° two-angle blade with variable bullnose.	38
Figure 4-8. Maximum insertion forces for all full-bullnose blades studied.	39
Figure 4-9. Maximum insertion forces for all non-bullnose blades studied.	39

Figure 4-10. Pebble displacement renders using X-PETS R2015b for $\Delta\text{Blade}=1d$ in a square 3100 instrumented pebble channel with side length $10.5d$ in a larger non-instrumented bed of $H=48d$. Pebbles and blade outline (green) shown in their final positions. Left: 45-degree 3-angle full bullnose blade. Middle: 45-degree 2-angle full bullnose blade. Right: 75-degree 3-angle full bullnose blade.....	40
Figure 4-11. Displacement vector fields showing the direction of pebble displacements using X-PETS R2015b for $\Delta\text{Blade}=1d$. Vector magnitudes are exaggerated to show detail.	41
Figure 4-12. Pebble displacements for the 45-degree 2-angle full bullnose blade represented as a histogram (left) and a probability density function (right). Generated using X-PETS R2015b for $\Delta\text{Blade}=1d$. Note the different binning configurations, the binning for the Weibull distribution plot is generated automatically by the distribution fitting algorithm.	42
Figure 5-1. Insertion force probability density function (left) and cumulative distribution function (right) for the 45-degree 3-angle full-bullnose blade being inserted into a pebble bed with height $48d$. Forces are scaled for a buoyant Mk1 PB-FHR pebble body force= 0.0302N	43
Figure 5-2. Effective lengths of columns with various boundary conditions [22].	45
Figure 5-3. Mk1 PB-FHR core dimensions [1]. Units in centimeters.	45
Figure 5-4. Solidworks model of the Mk1 PB-FHR control blade cross section and corresponding second (area) moments of inertia. X and Z moments are based on an arbitrary blade length.	46
Figure 5-5. Critical axial loads required for buckling as a function of unconstrained blade length for the three loading scenarios seen in Figure 5-2.....	47
Figure 5-6. Maximum blade deflection at the tip as a function of unconstrained blade length for three different loads. Left: uneven tip loading, equation (5.2). Right: uneven distributed loading, equation (5.4).	48
Figure 5-7. Insertion forces vs. blade insertion position ($z/d=0$ is where the blade initially contacts the pebble bed) for five pebble bed heights. Test performed with the 45° wedge insert and the 45° two-angle no-bullnose blade.....	49
Figure 5-8. Maximum insertion forces with one-sigma uncertainty vs. pebble bed height.....	49
Figure 5-9. Insertion profiles for four insertion velocities. Velocities are measured in pebble diameters per second.	51
Figure 5-10. Maximum insertion force for four insertion velocities. Tests performed using the 45-degree wedge, a pebble bed height of $48d$ and the 45-degree 2-angle full-bullnose blade.....	51

List of Tables

Table 2-1. Mk1 PB-FHR fuel pebble specifications [1].	15
Table 2-2. CoBIE/X-PREX pebble material specifications [5].	15
Table 2-3. Core flibe densities over the range of Mk1 PB-FHR core temperatures.	16
Table 2-4. Summary of scaling parameters.	17
Table 2-5. CoBIE test matrix.	22
Table 5-1. Best-estimate maximum diametrically compressive load limits calculated for a single 3.0-cm fuel pebble [21].	43
Table 5-2. Summary of relevant parameters for control blade buckling and deflection.	46
Table 5-3. Deflection of beams in loading conditions relevant to control blade insertion [22].	47
Table 5-4. CoBIE/X-PREX pebble surface static friction measurements [5].	52
Table 5-5. Graphite-on-graphite experimentally measured coefficients of friction in molten salt (FLiNaK) [13].	53
Table 5-6. CoBIE/X-PREX pebble mechanical contact measurements [5].	53

Acronyms and Abbreviations

CAD – Computer Aided Design
CDF – Cumulative Distribution Function
CoBIE – Control Blade Insertion Experiment
DAQ – Data Acquisition Device
DEM – Discrete Element Method
FHR – Fluoride Salt-Cooled High-Temperature Reactor
GUI – Graphical User Interface
HTR – High Temperature Reactor
HTGR – High Temperature Gas Reactor
PB-FHR – Pebble-Bed Fluoride Salt-Cooled, High-Temperature Reactor
PDF – Probability Density Function
THTR – Thorium High Temperature Reactor
UCB – University of California, Berkeley
USNRC – U.S. Nuclear Regulatory Commission
X-PETS – X-Ray Pebble Tomography Software
X-PREX – X-Ray Pebble Recirculation Experiment

1 Introduction to the Control Blade Insertion Experiment (CoBIE)

The control of reactivity in pebble bed reactors is complicated, and is generally achieved by inserting control elements into channels in the graphite reflectors that confine the pebble bed. Conversely, elements inserted directly into the pebble bed can have very high reactivity worth, but have the risk of damaging or breaking pebble fuel elements. In 2013, U.C. Berkeley developed designs for control blades that can be inserted directly into the pebble bed of the Mk1 Pebble-Bed Fluoride-Salt-Cooled High-Temperature Reactor (Mk1 PB-FHR) design [1][2]. The significant additional reactivity worth of these shutdown elements (compared to the control rods inserted into channels in the center graphite reflector) make them a highly desirable option for redundant and diverse shut down capabilities. The central reflector control rods, as well as the control blades (also called shutdown blades, which would be inserted directly into the pebble bed), can be seen in Figure 1-1 on the right.

The force imparted to pebbles by a control blade inserted directly into a packed bed is a very important parameter to determine the viability of this kind of shutdown system. The strategy of inserting control rods directly into a pebble bed core was adopted for the gas-cooled pebble bed Thorium High Temperature Reactor (THTR) in Germany (as seen in Figure 1-1, left), but for this gas-cooled design the forces imparted to pebbles led to a large number of broken pebbles, and complicated the initial operation of that facility [3]. In the salt-cooled pebble bed reactor designs, where pebbles have positive buoyancy and float against the upper reflector of the core, the insertion of a control blade from the top of the bed may prove to be more feasible due to the reduced body forces in the positively buoyant system and the lubricity provided by the coolant. In the case of core designs with an unconstrained free surface at the bottom of the bed, there are additional degrees of freedom for pebble motion that should also reduce the forces imparted to pebbles and the potential for damage.

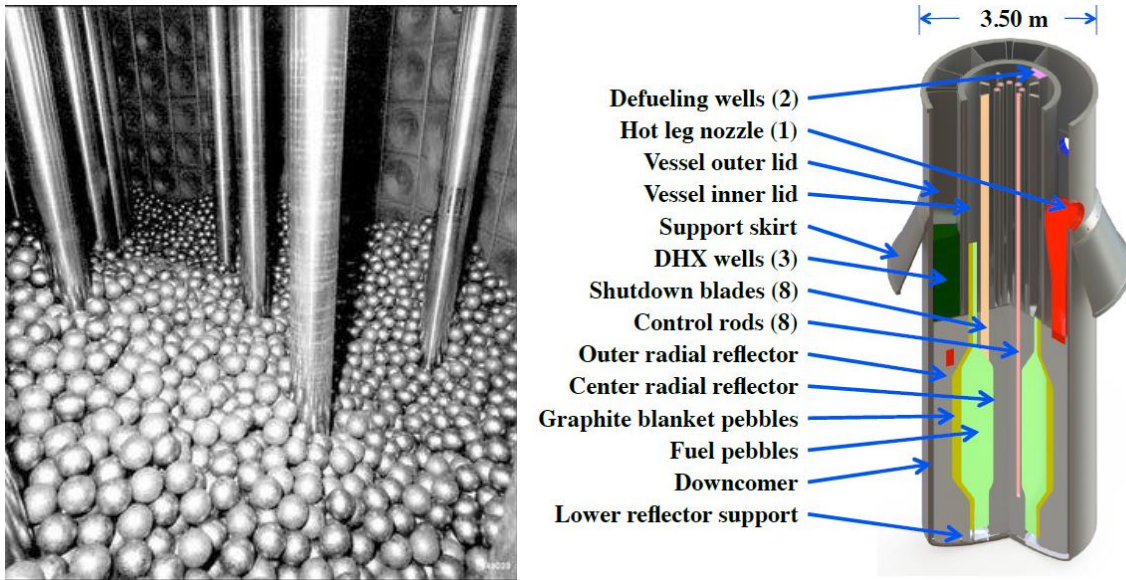


Figure 1-1. THTR core with control elements inserted [4] (left) and Mk1 PB-FHR core internals render [1] (right).

The X-ray Pebble Recirculation Experiment (X-PREX) facility at U.C. Berkeley is uniquely suited to study this safety-related design feature by measuring blade insertion forces and tracking the positions of individual pebbles as the control blade displaces them. These results can be used to validate Discrete Element Method (DEM) simulations, which can compute the forces on individual pebbles.

The Control Blade Insertion Experiment (CoBIE) was designed to examine the feasibility of blade insertion directly into a packed pebble bed. The experiment measures the insertion forces required to drive a control blade directly into a packed pebble bed, as well as the individual pebble displacements due to such an insertion. By doing this, the experiment helps to inform control blade and fuel element design unique to direct pebble bed insertion. This report describes the methodology behind the experiment, as well as the results.

2 Experimental Setup

The Mk1 PB-FHR core design consists of spherical graphite fuel elements cooled by a fluoride-lithium-beryllium molten salt commonly referred to as “flibe”, Li_2BeF_4 . The pebble fuel elements will float upwards due to their positive buoyancy in the high-temperature flibe. Control blades will be inserted from the top of the core directly into the pebble bed (in the direction of gravity), acting against the pebble buoyant force. To significantly simplify its design and operation, CoBIE is a dry experiment with control blades being inserted upwards into a pebble bed, against gravity. Spherical fuel elements are simulated in CoBIE using plastic spheres.

The X-PREX facility is uniquely suited for the operation of CoBIE [5]. The data acquisition (DAQ) system and the linear actuator control system provide the capability to drive the control blade insertion with precision linear motion, while gathering accurate insertion force measurements. Additionally, the X-Ray Pebble Tomography Software (X-PETS), which was developed at U.C. Berkeley specifically for use in the X-PREX facility, provides the novel capability of tracking individual pebble locations and rotation during a control blade insertion.

2.1 CoBIE Physical Description

CoBIE utilizes an acrylic test silo that can be combined with modular wedge inserts, a variety of control blade designs, and a packed pebble bed of variable height (Figure 2-1). The pebbles used for this experiment are 1.257 cm in diameter (approximately 0.5 inches) and are made of polyethylene. These pebbles are approximately 40% scale by length from the Mk1 PB-FHR design, which uses 3.0-cm diameter fuel pebbles. Additional 1.257cm polypropylene pebbles instrumented with a 0.33 mm diameter tungsten wire through the center are used to enable imaging with x-ray tomography.

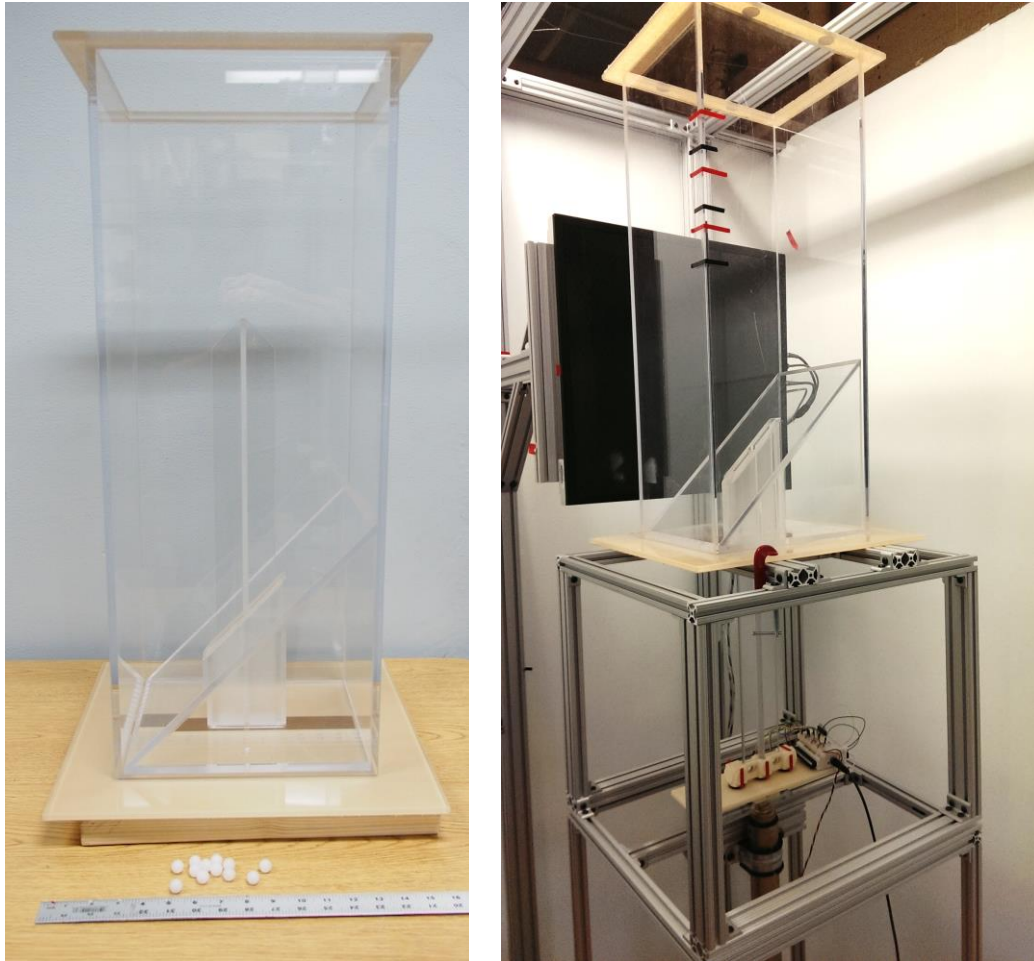


Figure 2-1. CoBIE test silo physical arrangement without a packed pebble bed. Left: acrylic test silo with 45-degree wedge insert, control blade, and instrumented pebbles. Right: acrylic test silo mounted on the X-PREX assembly with linear actuator retracted and x-ray detector in-view.

The CoBIE test silo has the option of two different wedge inserts. Each wedge offers a different pebble bed interface plane angle. One wedge has a pebble interface plane that is parallel to the horizon (the “0° wedge”, Figure 2-2 right). The other wedge has a pebble interface plane that is inclined at 45 degrees to the horizon (the “45° wedge”, Figure 2-2 left). The 45°-wedge represents the central reflector interface in an annular PB-FHR core. Both wedges have a Teflon sleeve that acts as a low-friction stabilizing channel for the control blade insertion path.

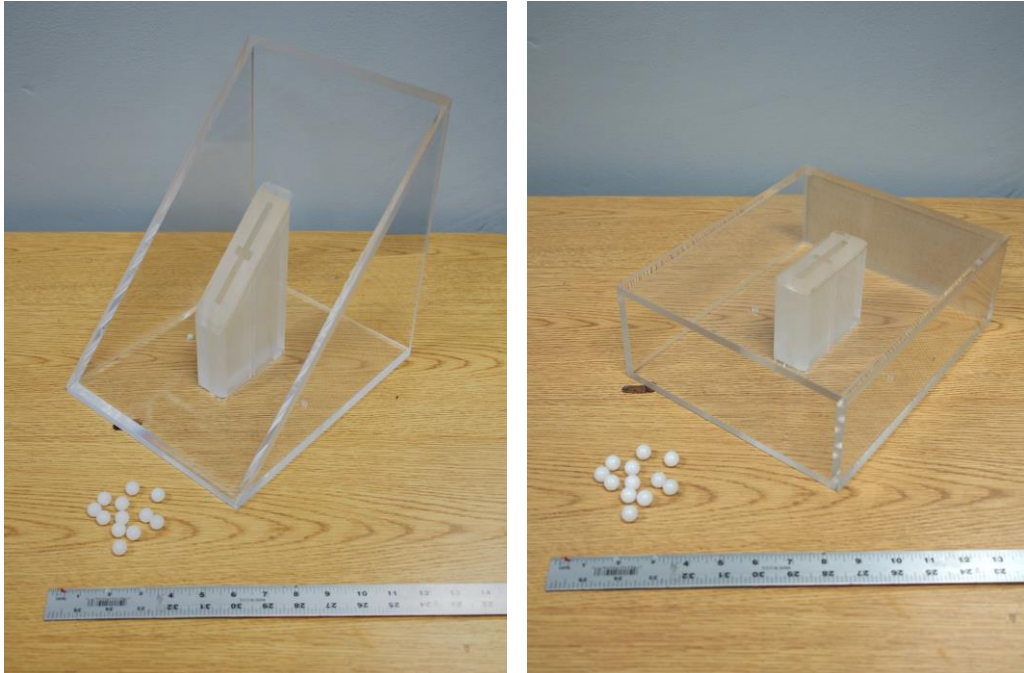


Figure 2-2. Detailed view of the modular inserts that feature Teflon sleeves for low friction blade insertion. Left: the 45-degree wedge. Right: the 0-degree wedge.

The primary blade design consists of a flat blade with stiffening ribs, creating a cruciform cross section (Figure 2-3). The thickness of the flat blade without stiffening ribs is equal to half of a pebble diameter in both the Mk1 PB-FHR and CoBIE systems (40% length scale in CoBIE). In the CoBIE system, the scaled cruciform blade is designed such that it can be fabricated out of 0.635 cm (0.25 in) polycarbonate sheets. The blades are designed to optimize pebble flow around the blades, which would be the case of a defueling procedure during shutdown. The pebbles will flow around the blade without trapping, due to the blade’s narrow cross-sectional area. Additionally, the blades are hypothesized to minimize pebble displacement during a control blade insertion event. The initial blade design was proposed by Chang et al., and was shown to be a viable design based on initial tests [2].

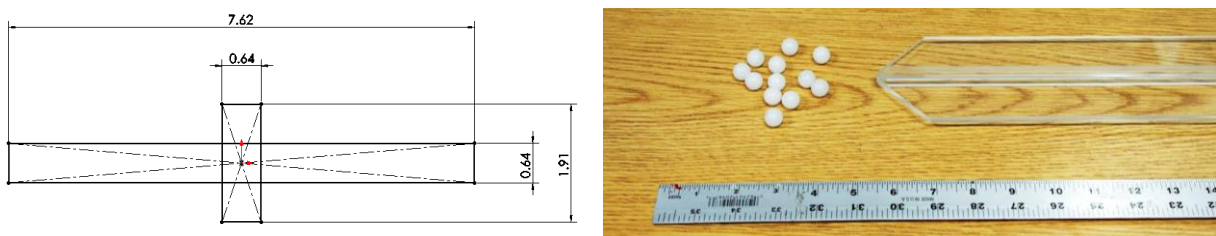


Figure 2-3. Primary control blade design. Left: cruciform cross section (dimensions in centimeters). Right: Actual blade compared to the 1.257 cm diameter pebbles.

The two main blade-geometry designs studied consist of a tip with two variable angles, and a tip with three variable angles, as shown in Figure 2-4. The naming convention is perhaps not so intuitive, so it is important to note that the blade tip with two variable angles has a third angle that is constrained at 90-degrees. It is also important to note that the designated angle of a blade

tip is measured from the horizontal, such that a 30° blade is blunt compared to a 60° blade. Figure 2-4 shows the naming convention and tip geometries for 30° two-angle and three-angle blades.

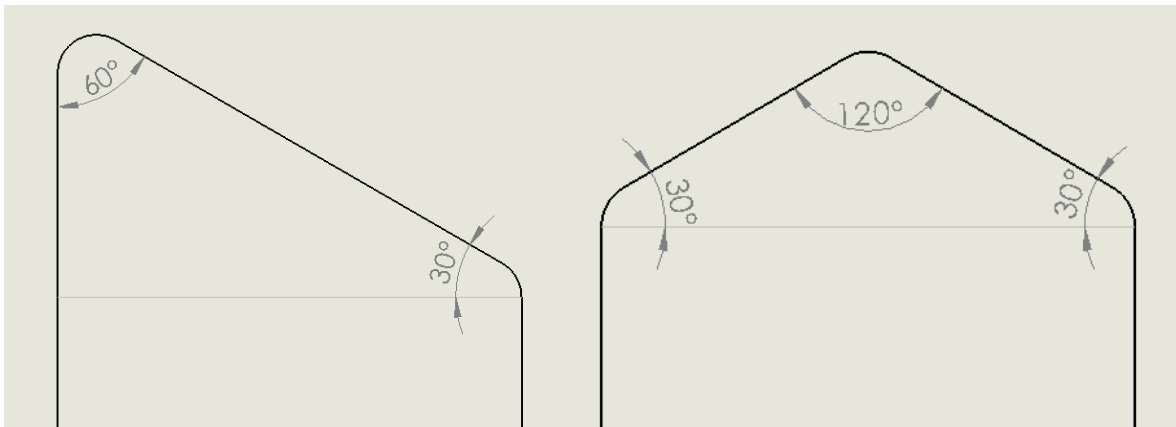


Figure 2-4. Two blade geometries with annotations showing the unconstrained angles in the tip. Left: 30-degree two-angle blade. Right: 30-degree three-angle blade.

One additional novel blade geometry tip was tested. The original theory was that the sharpest blade would require the least amount of force to insert into a packed pebble bed. However, a concern was raised that a blade with too sharp of a tip would not have sufficient structural integrity. Therefore, a modified blade tip was designed with five tip angles to yield a sharp tip, with a blunt base. This blade can be seen in Figure 2-5, and will be referred to as the 5-angle blade.

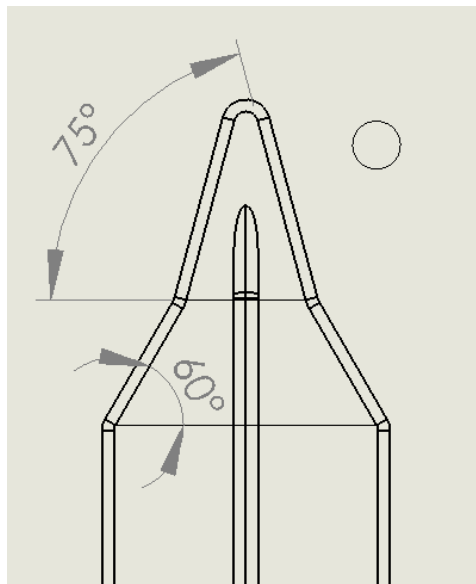


Figure 2-5. 5-angle blade tip with a pebble diameter shown as a circle for scale.

Another blade tip parameter studied is the degree to which the blade corners are rounded. A blade with fully rounded corners (radius equal to half of the blade thickness) is referred to as a full bullnose, and corners with only 90° angles is referred to as having no bullnose. Half bullnose

corners (radius equal to a quarter of the blade thickness) were also studied. Three blade tips with varying bullnose can be seen below in Figure 2-6.

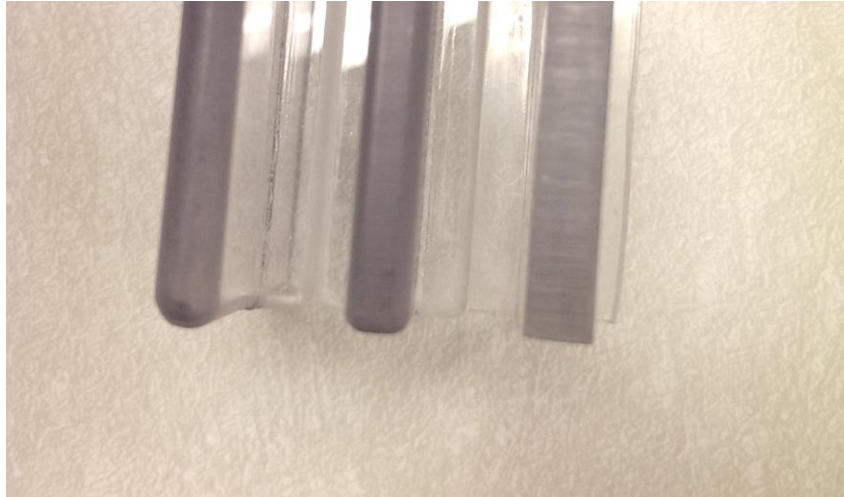


Figure 2-6. Three blade tips with a full bullnose (left), half bullnose (middle) and no bullnose (right).

2.2 Notes on CoBIE Scaling

CoBIE was designed with consideration for how pebble contact forces and blade insertion forces will scale to a real reactor system. The length scale of CoBIE is approximately 40% of the Mk1 PB-FHR design, yielding a convenient laboratory scale (Table 2-1, Table 2-2). Length dimensions are nondimensionalized using the pebble diameter d to yield position coordinates that can easily be applied to a reactor system. Common notation in this report is to represent the Cartesian coordinate system as x/d , y/d or z/d , signifying the length along a given axis, divided by one pebble diameter.

Table 2-1. Mk1 PB-FHR fuel pebble specifications [1].

Fuel pebble design	
Pebble diameter	30.0 mm
Graphite coating thickness	1.0 mm
Inner graphite core diameter	25.0 mm
Uranium enrichment	19.9%
Pebble heavy metal loading	1.5 gHM
Carbon to heavy metal ratio	300
Number of coated particles per pebble	4730
Coated particle packing fraction in fuel layer	40%
Average pebble thermal power	500 W
Average pebble density	1745 kg/m ³
Average pebble full-power lifetime	1.40 yr
Fuel kernel design	
Fuel kernel diameter	400 μm
Fuel kernel density	10,500 kg/m ³
Fuel kernel composition	UC _{1.5} O _{0.5}
Buffer layer thickness	100 μm
PyC inner layer thickness	35 μm
SiC layer thickness	35 μm
PyC outer layer thickness	35 μm

Table 2-2. CoBIE/X-PREX pebble material specifications [5].

	Unmodified	Instrumented
Pebble Material	Polyethylene	Polypropylene
Plastic Density [g/cm ³]	0.96	0.9
Pebble Diameter [cm]	1.257	1.257
Pin Material	-	Tungsten
Metal Density [g/cm ³]	-	19.25
Pin Diameter [cm]	-	0.013
Pebble Density [g/cm ³]	0.96	0.96
Image Width [Pixels]	-	3

CoBIE forces are nondimensionalized by a single pebble body force. These units, represented typically as F/mg , can easily be applied to a reactor with buoyant pebble fuel where mg is the body force (buoyant minus gravity) on a single pebble. The granular drag phenomena observed in a media pebble bed cannot be described by a classical continuum scaling methodology, so a simplistic scaling methodology is employed. The methodology to this approach is described as follows.

It becomes necessary to consider exactly how the motion of a blade inserted into a packed pebble bed is resisted. Granular jamming effects have previously been studied as an effect of inhomogeneous stress propagation through stress chains of strained grains [7]. Overcoming such jamming effects requires the large-scale reorganization of the granular bed [7]. In an analogous

manner, an object (a control blade, in this experiment) moving through a packed pebble bed can only persist by inducing the same large-scale granular reorganizations [8]. Objects being dragged through a granular bed must reorganize the granular bed structure through creation and subsequent destruction of stress-chains in the granular media.

The Coulombic friction model in cohesion with hydrostatic bed pressure have been used to describe the creation and propagation of stress chains in granular media [9][10][12]. Both the Coulombic friction force and the hydrostatic bed pressure are caused directly by the multitude of pebble body forces. Additionally, the force on an object being dragged through a granular bed has been described as a linear function of the individual pebble body force and the individual pebble surface properties [10].

It is therefore logical to nondimensionalize blade insertion force by a single pebble body force, as the granular resistance to motion is directly proportional to the granular media's body force.

The body forces on both the Mk1 PB-FHR fuel pebbles must be calculated to find the appropriate force scaling factor. The body force on a CoBIE pebble is calculated as follows:

$$F_{CoBIE} = V \rho g = \frac{4}{3} \pi \left(\frac{0.01257m}{2} \right)^3 \left(960 \frac{kg}{m^3} \right) \left(9.8 \frac{m}{s^2} \right)$$

$$F_{CoBIE} = 0.0098N$$

Equation (2.1) calculates the density of flibe as a function of temperature [6]:

$$\rho_{flibe} \left[\frac{kg}{m^3} \right] = 2280 - (0.488 \times T(^{\circ}C)) \quad (2.1)$$

The density of flibe calculated over the range of Mk1 PB-FHR core temperatures is calculated using equation (2.1) and displayed in Table 2-3.

Table 2-3. Core flibe densities over the range of Mk1 PB-FHR core temperatures.

Temperature [°C]	Flibe Density [kg/m ³]
600 (Core Inlet [1])	1987.2
650 (Approximate Core Avg [1])	1962.8
700 (Core Bulk-Average Outlet [1])	1938.4

For this analysis, flibe density is taken at 650°C, which is the average bulk temperature of the Mk1 PB-FHR core [1]. The Mk1 pebble body force can be calculated using equation (2.2):

$$F_{PB-FHR} = V_{pebble} g (\rho_{flibe} - \rho_{pebble}) \quad (2.2)$$

The body force evaluated for a Mk1 PB-FHR pebble in 650°C FLiBe is calculated here:

$$F_{PB-FHR} = \frac{4}{3} \pi \left(\frac{0.03m}{2} \right)^3 \left(9.8 \frac{m}{s^2} \right) \left(1962.8 \frac{kg}{m^3} - 1745 \frac{kg}{m^3} \right)$$

$$F_{PB-FHR} = 0.0302N$$

The experimentally measured insertion forces are divided by the body force on a CoBIE plastic pebble to yield non-dimensional units of F/mg . Dimensional insertion forces for the Mk1 PB-FHR design are then calculated by multiplying by the buoyant Mk1 PB-FHR pebble body force.

The resulting body force scaling factor is calculated to be:

$\frac{F_{PB-FHR}}{F_{CoBIE}} = \frac{0.0302}{0.0098} = 3.08$

Based on the granular drag discussion by Albert et al. [10], the critical force for an object to reorganize a granular bed (and therefore the granular drag and blade insertion forces) is directly proportional to the body force acting on a single grain (or pebble). The above-calculated pebble body force scaling factor can therefore be used to scale the blade insertion forces measured by CoBIE to a real reactor system. CoBIE results will be nondimensionalized by a single CoBIE pebble body force, and then (in section 5.1) multiplied by the Mk1 PB-FHR body force to yield dimensional results.

Albert et al. shows (experimentally) that the drag force is also proportional to the surface characteristics of individual pebbles. For this analysis, the surface characteristics are assumed constant between the CoBIE results and the actual reactor system. The accuracy of this approximation is discussed in relation to the CoBIE results in section 5.3 of this report.

Table 2-4 summarizes the scaling parameters used in this report, as well as some of the scaling parameters that could be used to relate the results in this report to different pebble bed reactor systems. High Temperature Gas-Cooled Reactor (HTGR) pebble properties are taken from the HTR-10 program in China [11]. The 6cm pebble in molten salt coolant is relevant for the Shanghai Institute of Applied Physics (SINAP) Thorium Molten-Salt Reactor Solid Fuel (TMSR-SF) program. The SINAP TMSR-SF pebble properties are assumed to be similar to the HTR-10 pebbles, with molten salt coolant properties assumed to be similar to flibe at 650°C.

Table 2-4. Summary of scaling parameters.

	CoBIE	Mk1 PB-FHR	SINAP TMSR-SF	HTR-10 Pebble
Pebble Diameter (m)	0.01257	0.030	0.060	0.060
Pebble Density (kg/m ³)	960	1745	1760	1760
Coolant Density (kg/m ³)	Negligible	1962.8	1962.8	Negligible
Single Pebble Body Force (N)	0.0098	0.0302	0.2414	1.9507

Force Scaling Factor (Reactor/CoBIE)	1	3.08	24.63	199.05
--------------------------------------	---	------	-------	--------

2.3 Controls and Sensors

The linear actuator, which drives the control bade into the pebble bed, is actuated using a relay switch controlled by a National Instruments (NI) DAQ-6009. The position of the actuator can be measured with sub-millimeter precision using a potentiometer built into the actuator. Blade insertion forces are measured using three Tekscan FlexiForce A401 piezoresistive force sensors. Rubber bumpers are glued to either side of the force sensors for uniform load distribution. Each force sensor is wired using circuitry recommended by the manufacturer to return a linear force-voltage relationship. The force sensor output voltages are measured using another NI DAQ-6009, which is kept separate from the DAQ-6009 that controls the linear actuator, in order to eliminate electrical noise.

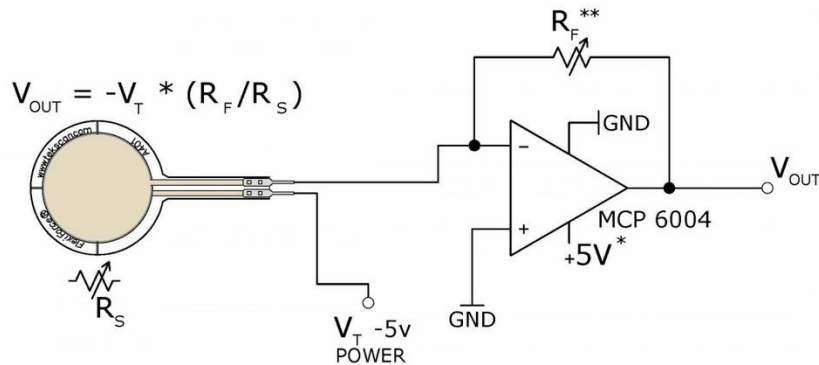


Figure 2-7. Wiring schematic for the force sensors. Voltage probe is representative of the DAQ-6009.

Samples are collected at a rate of 10,000 samples per second per sensor by a custom NI LabVIEW Virtual Instrument (VI). The VI records approximately 15 data points per second. Each data point consists of a moving average of 500 samples, in order to eliminate electrical noise for a more accurate measurement.

The three force sensors are calibrated using a 17 point calibration test. Weights are loaded on a blade cradle with the sensors adhered to the bottom, as would be the loading scenario in actual experiment. The calibration can be seen below in Figure 2-8. The standard deviation from the linear fit is 326 pebble masses. This standard deviation will be reduced to one significant figure, as per the standard representation of uncertainty, once combined with the experimental uncertainty. This sensor uncertainty can be attributed to three independent sensors acting in parallel with their own respective uncertainties being superimposed, as well as imperfect force loading conditions.

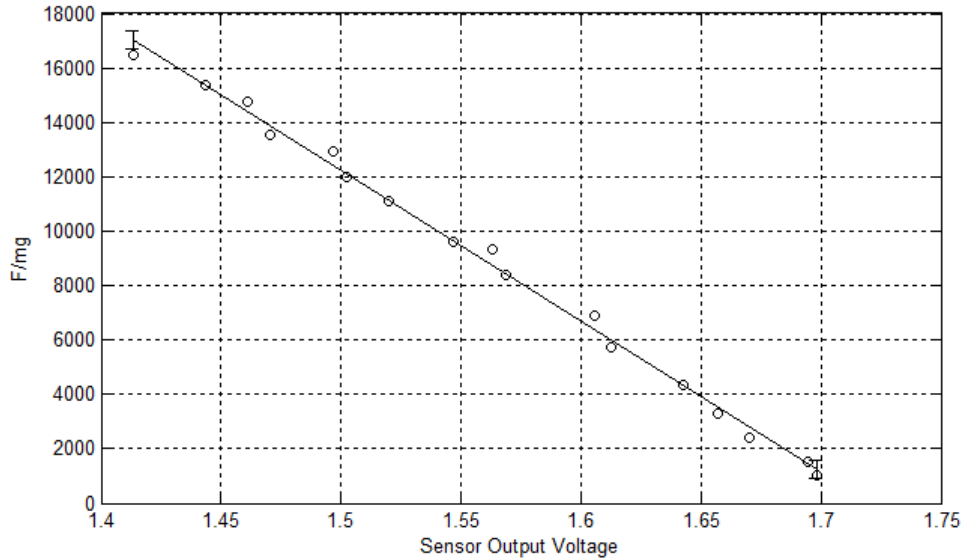


Figure 2-8. 17-point calibration of three Tekscan FlexiForce A401 Sensors with resulting fit function. Error bars show one standard deviation (326 pebble masses).

During the experiment, the three force sensors are used to measure the vertical insertion force of the blade into the pebble bed. The force sensors are arranged in parallel in an interface between the actuator and the control blade (Figure 2-9). Multiple sensors are used to ensure that each sensor is operating within its maximum force limit.

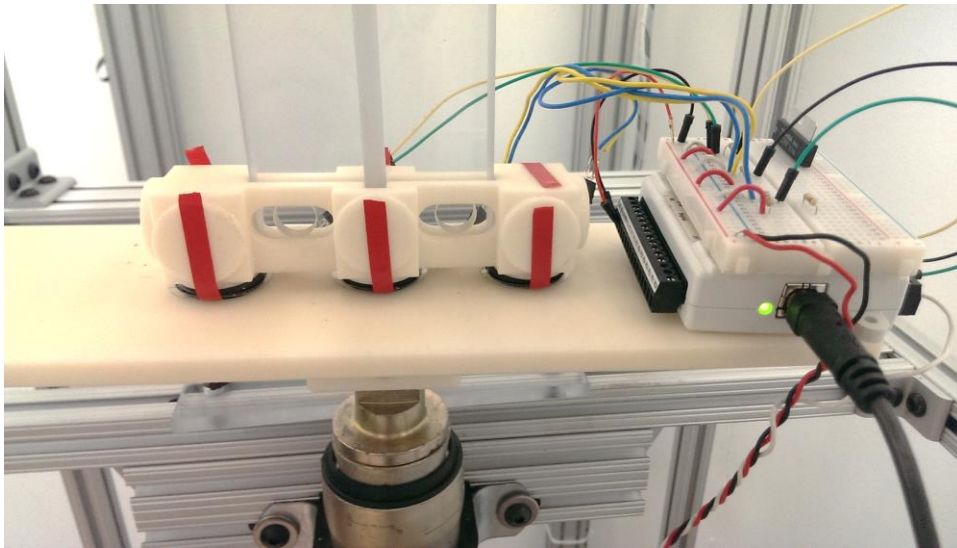


Figure 2-9. Detailed view of force sensor setup during an experiment.

The 3D-printed interfaces (beige-colored in Figure 2-9) create parallel contacts between the blade and the actuator for nominal force sensor contact. Blue and yellow wires lead to the three force sensors. The device on the right in Figure 2-9 is the NI DAQ-6009 device with a wiring breadboard mounted on top.

The assembly was made such that two of the force sensors could be rearranged on the top of the blade cradle. By doing this, the force required to retract a blade from a packed pebble bed can

also be measured. A two-sensor calibration is performed for these tests, and can be seen in Figure 2-10. A smaller uncertainty for the two sensor calibration supports the claim that using more force sensors in parallel creates additional uncertainty in the measurement.

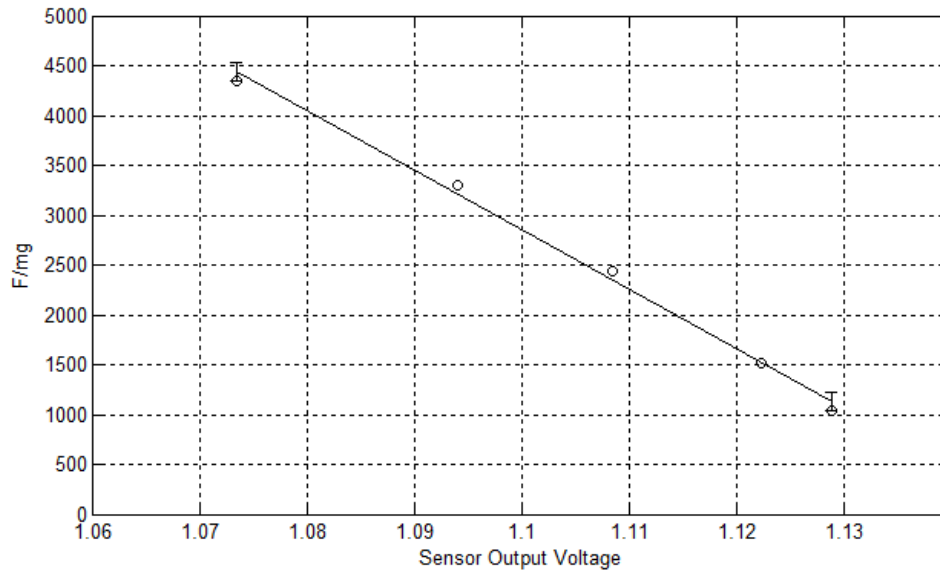


Figure 2-10. Five-point calibration of two Tekscan FlexiForce A401 Sensors for retraction force tests. Linear fit is shown with one-sigma error bars (90 pebble masses).

2.4 Experimental Procedure

There are two separate procedures for tests that collect insertion forces, and for tests that collect x-ray images for tomography.

2.4.1 Insertion Force Test Procedure

For tests that collect only blade insertion force data, the LabVIEW control VI is the only necessary piece of software.

Before starting an experiment, the operator verifies that the actuator and force sensors are properly connected and powered. The operator sets an extension limit on the actuator (using the custom LabVIEW control VI), so that the actuator does not drive the blade too far and damage the test silo. The operator then fills the test silo with pebbles until the desired pebble bed height is reached. Pebbles are poured into the silo to create a random packing distribution. Pebble bed heights are measured from the center point of blade entry to the approximate maximum height of the pebble bed. The friction force caused by the blade sliding through the Teflon sleeve is measured independently from the force exerted by the pebbled bed, before the blade contacts the bed. This friction force was found to be small, and is subtracted from the measured insertion force profile.

The operator uses the LabVIEW VI to simultaneously actuate the linear actuator, driving the blade into the pebble bed, while recording data from the two force sensors. The extension limit

automatically stops the blade insertion at the programmed stopping point. The recorded data is exported to Microsoft Excel using LabVIEW's built in features.

Before performing another experiment, the operator must completely empty and refill the test silo with pebbles. Performing subsequent blade insertions without completely emptying and refilling the pebbles dramatically affects insertion forces, as can be seen in section 4.1.

2.4.2 Pebble Tomography Experimental Test Procedure

For tests that collect x-ray images, the procedure is modified slightly. Instrumented pebbles are used for pebble tracking in the x-ray images. Because the pebbles close to the blade insertion path are the pebbles of interest, a column of instrumented pebbles is placed over the insertion region, as seen in Figure 2-11. The instrumented column is kept separate from the rest of the bed by a cardboard channel, which is removed before the test. For the experiments documented in this report, the channel of instrumented pebbles has a square cross section with a side length $10.5d$. Any ordered packing effects are expected to disperse when the cardboard channel is removed.

The additional pieces of software required are the turntable control software, the x-ray image acquisition software, and X-PETS and along with post processing modules.

Once the silo is filled, the data collection can begin. While collecting x-ray images, the blade is inserted in a stepwise fashion in motion steps of $\frac{1}{4}$ of a pebble diameter. At every blade insertion position, the test silo is rotated to five different angles using the turntable software. X-ray images are collected at each rotational angle. Once all images are collected for a given motion step, the blade is inserted one additional motion step. The magnitude of a motion step can be changed in the LabVIEW control VI. X-ray images are then collected at the new motion step.

This procedure is repeated until the blade is fully inserted and five x-ray images have been collected at five different angles for each motion step.

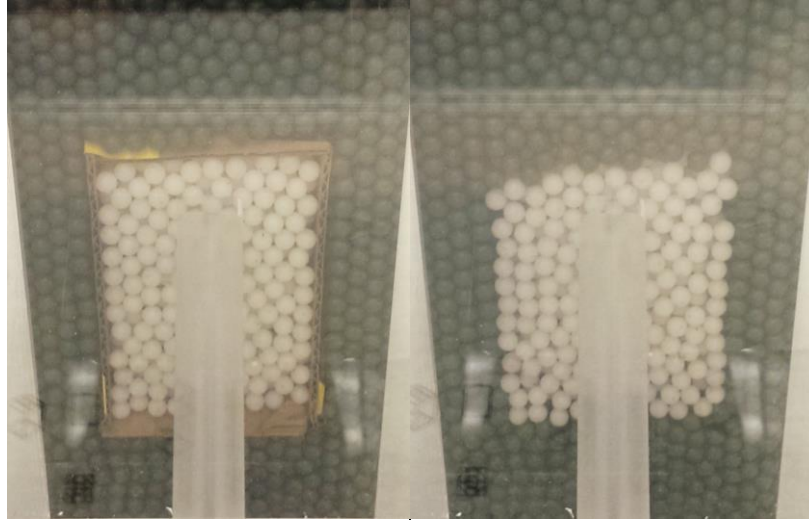


Figure 2-11. Sheath of instrumented pebbles (white) surrounded by non-instrumented pebbles (green) for a localized tomography study. Left image shows cardboard divider used to segregate pebble regions. Right image shows bed after the divider is removed.

2.5 Test Matrix

The CoBIE setup utilizes modular components, allowing for many degrees of freedom. A summary of the possible tests can be seen in Table 2-5 below. Completed tests are marked with a check-mark.

Table 2-5. CoBIE test matrix.

	45 Degree Wedge Insert	Bullnose vs. No Bullnose	Variable Pebble Bed Height	Secondary Insertions	Variable Speed Insertion
0 Degree Flat Tip	✓	✓			
30 Degree 3-Angle	✓	✓			
45 Degree 3-Angle	✓	✓			
60 Degree 3-Angle	✓	✓			
75 Degree 3-Angle	✓				
30 Degree 2-Angle	✓	✓			
45 Degree 2-Angle	✓	✓	✓	✓	✓
60 Degree 2-Angle	✓	✓			
75 Degree 2-Angle	✓				
5 Angle Blade Tip	✓		✓		

The tests seen completed in Table 2-5 measured insertion forces and did not perform x-ray tomography. Because of the time intensive nature of the tomography tests, only a subset of the tests seen in Table 2-5 were performed with x-ray tomography. Specifically, the 45-degree 2-

angle full-bullnose, the 45-degree 3-angle full-bullnose and the 75-degree 3-angle full-bullnose were tested using x-ray tomography.

3 Data Analysis Techniques

3.1 Insertion Force Profiles

3.1.1 Maximum Insertion Force and Uncertainty Analysis

The motion of a control blade through a packed pebble bed is analogous to previous experiments performed on the granular drag of a discrete object [8]. In such experiments, an object's motion is resisted by the jamming of grains. Jamming is caused by networks of stress chains in the granular bed that are continually broken by the object's motion.

In a randomly packed pebble bed, such as the pebble bed core of the PB-FHR, the resistance to an object's motion is stochastic in nature. Of particular concern for this experiment is the maximum force required to insert a control blade into such a pebble bed. The maximum force dictates both the operational requirements of the safety system, as well as the mechanical requirements of the fuel, which must be subjected to this insertion force.

The maximum force must be calculated with consideration for the stochastic nature of the insertion force profile. Simply taking a single maximum force of a given data set is an inherently flawed methodology. Performing such an analysis grossly neglects much of the data.

One methodology employed in this experiment selects the five peak forces in a given insertion force profile, with the average and standard deviation of this subset yielding the maximum force with uncertainty.

Two typical insertion force profiles with the maximum insertion forces according to this methodology can be seen in Figure 3-1. The calculated average maximum forces and their respective uncertainties can be seen to be a good representation for the maximum required insertion forces for these experiments.

Figure 3-2 shows the results of this methodology for five identical experiments. The repeatability of this maximum insertion force methodology verifies that it is an appropriate method.

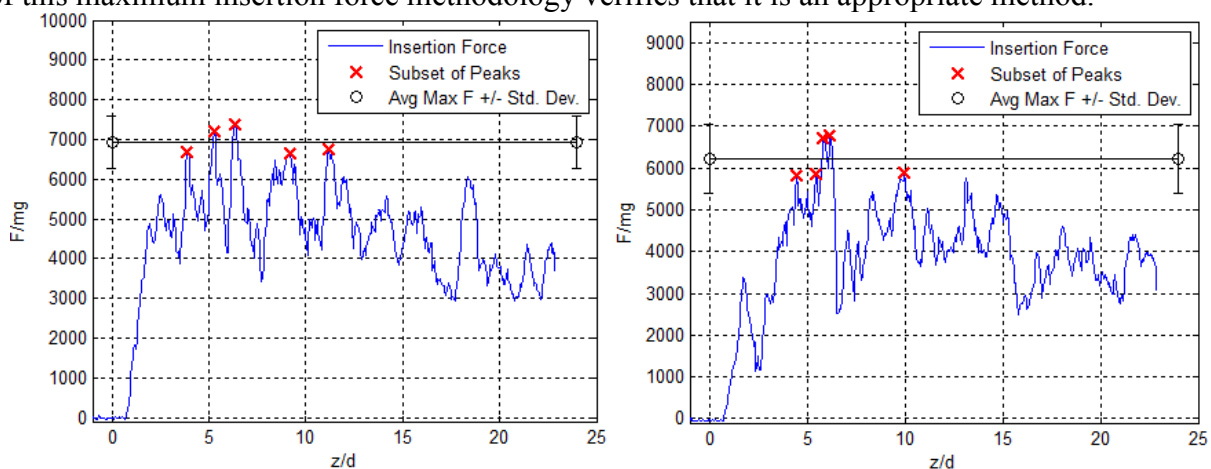


Figure 3-1. Typical insertion force profiles with average maximum force and one-sigma uncertainties calculated from five peak forces. Sensor uncertainty is included in the

standard deviations. Tests performed with the 45-degree wedge, pebble bed height of 48d, and the 45-degree two-angle full-bullnose blade.

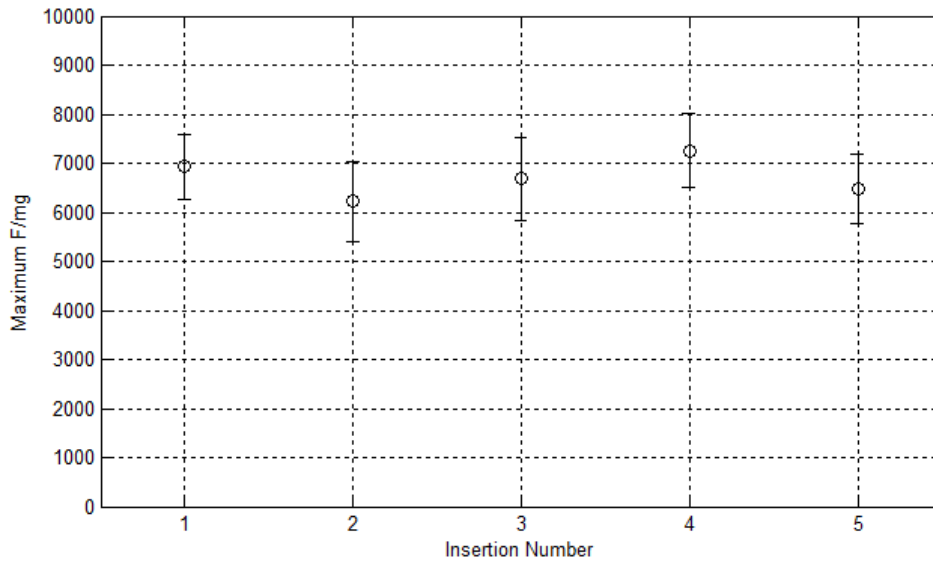


Figure 3-2. Maximum force methodology for five identical experiments. Insertion velocities=0.803 ± 0.014 d/s. All tests performed with the 45-degree wedge, pebble bed height of 48d, and the 45-degree two-angle full-bullnose blade.

Many CoBIE tests are well represented by plotting the maximum insertion force as a function of an independent variable. For these results, the aforementioned maximum force methodology is used. Two-dimensional trends are shown to be well visualized by this methodology.

3.1.2 Treatment of Insertion Forces Using the Weibull Distribution Function

One of the primary motivations for CoBIE is to be able to assess the probability of maximum insertion forces as well as the probability of maximum contact force on a given pebble. For this reason, a probabilistic approach is explored as a method to interpret results.

Extreme value statistics [14] is proposed as the appropriate family of statistical distributions for these data sets. Specifically, the Weibull distribution can be shown to be in very good agreement with the insertion force data. Weibull distributions are routinely applied to describe material failure probability.

In order to apply Weibull distributions to the insertion force data sets measured by CoBIE, a subset of the insertion force data is selected. The insertion force subset is chosen to represent the fully-developed maximum insertion force distribution. Insertion forces early and late in the insertion force profile are typically excluded, because they are expected not to accurately contribute to the maximum force distribution. Subsets of insertion force data compared to full insertion force profiles can be seen in Figure 3-3. The two insertion force profiles seen in Figure 3-3 correspond to the insertion force profiles seen in Figure 3-1.

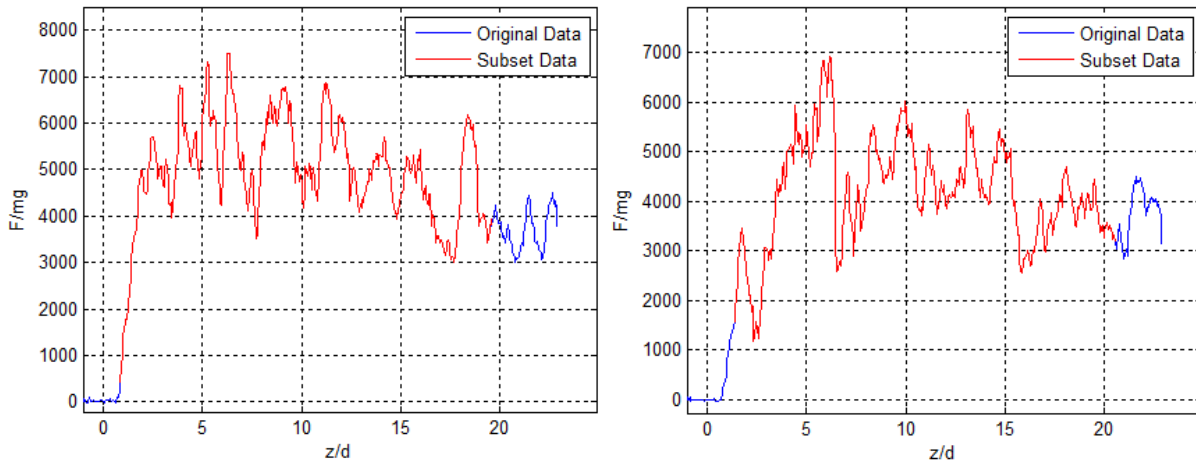


Figure 3-3. Force profile data subset selection for Weibull statistics. Tests performed with the 45-degree wedge, pebble bed height of $48d$, and the 45-degree two-angle full-bullnose blade.

The insertion force data subsets can be shown to be in very good agreement with Weibull probability distributions. For the analysis in this study, the MATLAB “probplot.m” function is used to show the correlation between the measured data and six distribution types. The distribution types considered are: exponential, extreme value, lognormal, normal, Rayleigh and Weibull distributions. The Weibull distribution is shown to be a very good fit for the data subsets, as seen in Figure 3-4. There is considerable deviation from the Weibull distribution at low forces, but this is considered acceptable because of the insignificance of small insertion forces. The five tests in Figure 3-4 correspond to the five tests in Figure 3-2.

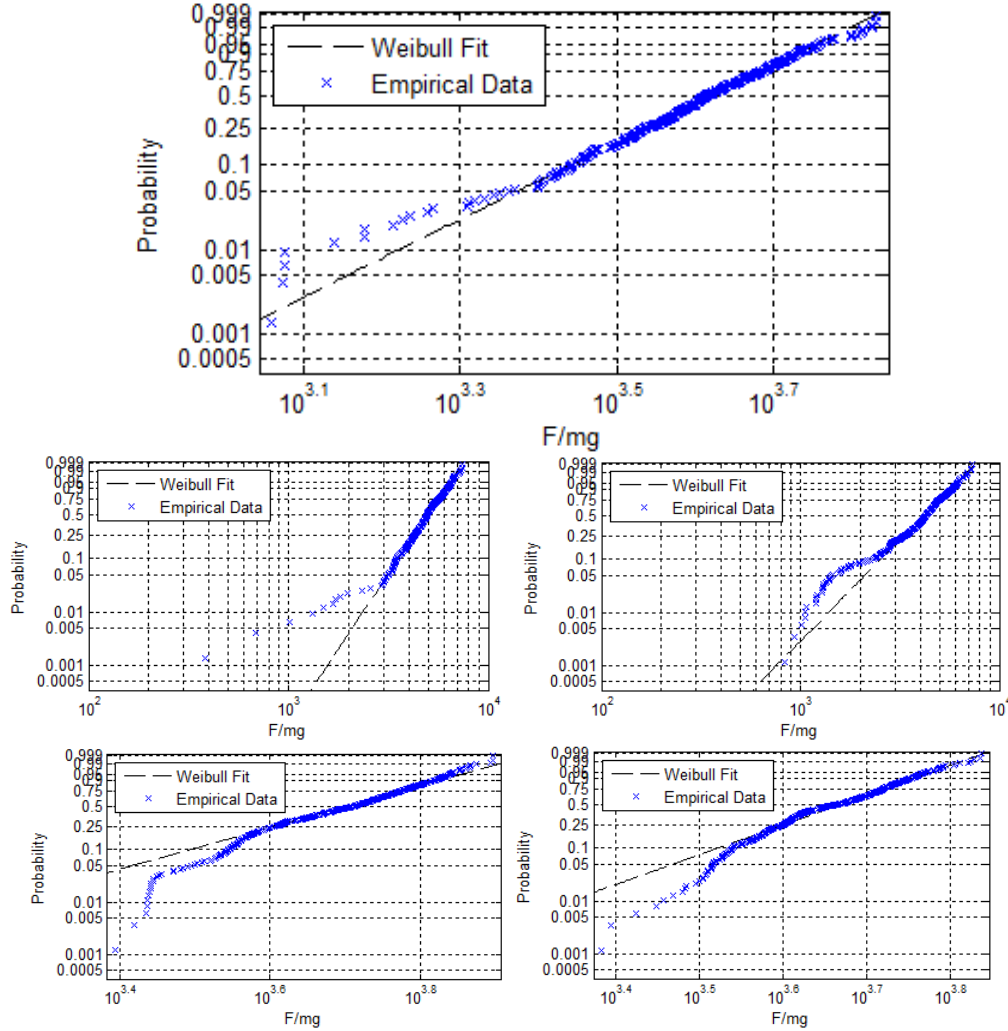


Figure 3-4. Weibull correlations for five identical blade insertion experiments. Insertion velocities= 0.803 ± 0.014 d/s. All tests performed with the 45-degree wedge, pebble bed height of $48d$, and the 45-degree two-angle full-bullnose blade.

After verification that the Weibull correlation is an appropriate distribution function, fit parameters can be determined to analytically describe the data. The two fit functions used are the Weibull Probability Density Function (PDF) and the Weibull Cumulative Distribution Function (CDF). The PDF function is defined as follows for $x > 0$ [14]:

$$PDF(x) = \frac{k}{\lambda} \left(\frac{x}{\lambda}\right)^{k-1} \exp\left(-\left(\frac{x}{\lambda}\right)^k\right) \quad (3.1)$$

Where

- $PDF(x)$ is the probability density for a given parameter x .
- x is the independent variable.

- k is the shape parameter, which adjusts the skew of the PDF.
- λ is the scale parameter.

It is important to note that the Weibull PDF is normalized to the area under the distribution. That is to say that integrating the PDF from $x = 0$ to $x = \infty$ returns unity. This also implies that integrating the PDF over a certain range of x yields the probability of measuring a data point in that range of x .

The Weibull CDF function is defined as follows [14] with the same shape and scale parameters as in (3.1):

$$CDF(x) = 1 - \exp\left(-\left(\frac{x}{\lambda}\right)^k\right) \quad (3.2)$$

Where $CDF(x)$ is the cumulative distribution function as a function of the independent variable x for $x > 0$.

Equations (3.1) and (3.2) can be seen fit to an empirical insertion force data subset (the data subset shown on the right in Figure 3-3):

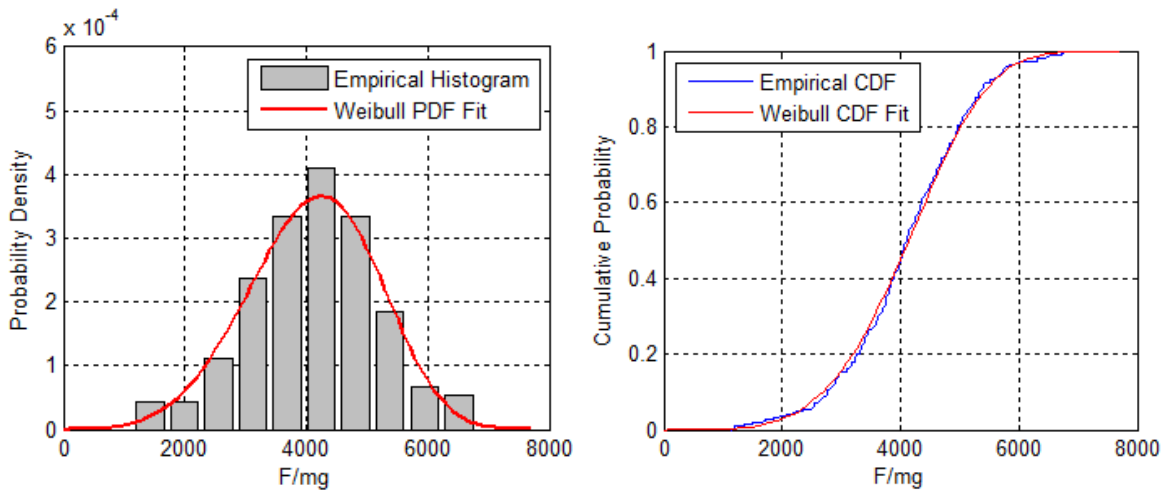


Figure 3-5. Weibull probability density function (left) and cumulative distribution function (right). Test performed with the 45-degree wedge, pebble bed height of 48d, and the 45-degree two-angle full-bullnose blade.

Figure 3-5 verifies that the Weibull distribution is an accurate representation of the empirically measured insertion force data. Weibull PDF and CDF analytic fit functions can be seen in Figure 3-6 and Figure 3-7 for five identical blade insertion experiments.

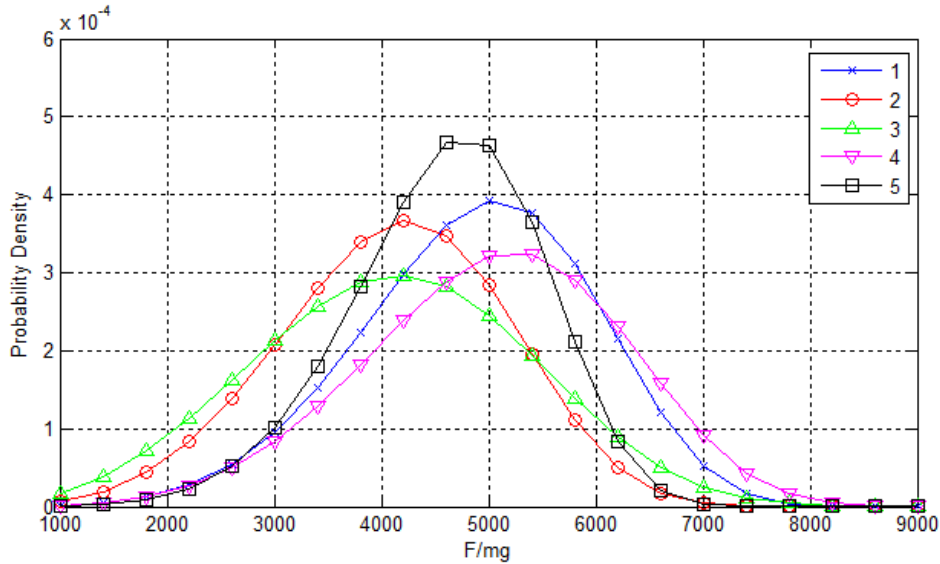


Figure 3-6. Five Weibull PDFs for five identical blade insertion experiments. Insertion velocities= 0.803 ± 0.014 d/s. All tests performed with the 45-degree wedge, pebble bed height of $48d$, and the 45-degree two-angle full-bullnose blade.

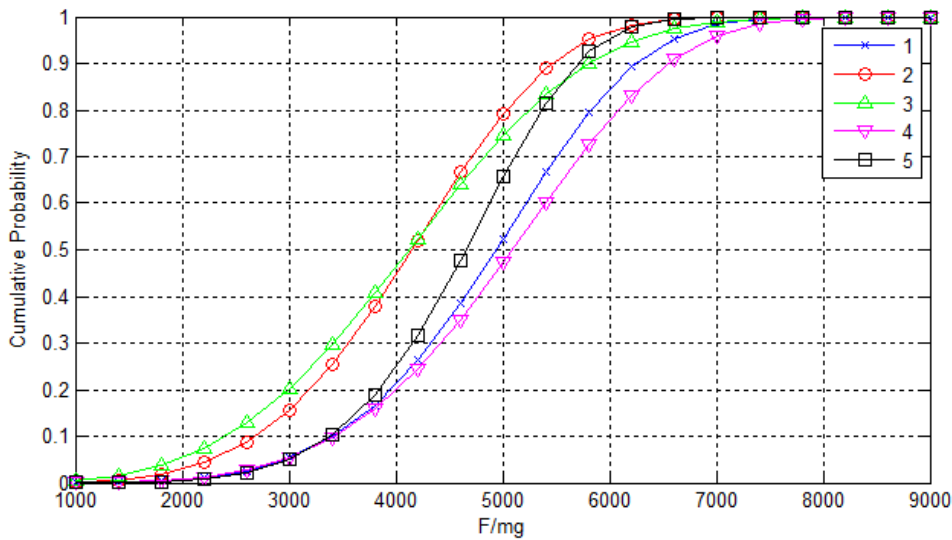


Figure 3-7. Five Weibull CDFs for five identical blade insertion experiments. Insertion velocities= 0.803 ± 0.014 d/s. All tests performed with the 45-degree wedge, pebble bed height of $48d$, and the 45-degree two-angle full-bullnose blade.

The Weibull distribution is a powerful tool for assessing the relative probability of insertion forces. This probabilistic treatment of data will also be used to describe pebble displacement probability using the x-ray tomography software.

3.2 X-PETS Data and CoBIE Custom Post Processing Module

The X-PETS R2015b software program processes image data to locate and track instrumented pebbles with both three axis of centroid position and two axes of rotational position. Initial experiments are returning pebble tracking efficiencies over 90% with high accuracy. Methods for assessing the uncertainties in the tomography results are still being developed. For this reason, results in the section are not displayed with uncertainties or error bars. It is important to note however, that initial measurements indicate tomography location data with uncertainties of less than 10% of a pebble diameter (less than a millimeter).

X-PETS R2015b was used to track how pebbles are displaced as a result of control blade insertion. One of the main concerns that CoBIE results provide insights for is fuel damage. X-PETS allows the novel ability to experimentally see inside a scaled pebble bed core, and examine how individual pebbles react to the insertion of a control blade. While X-PETS cannot measure contact forces on individual pebbles, the output data can be used to validate DEM simulations (such as LAMMPS) which can assess the probability of fuel failure through individual contact forces. This data can also lead to operational requirements of PB-FHR fuel elements, similar to those guidelines set forth for HTR's [15].

Figure 3-8 shows a typical experimental set up for a CoBIE pebble tomography experiment. A channel of instrumented pebbles is placed over the blade entrance. The instrumented pebbles can be seen in the x-ray images by the tungsten wire running through their center (the cluster of white lines in Figure 3-8).

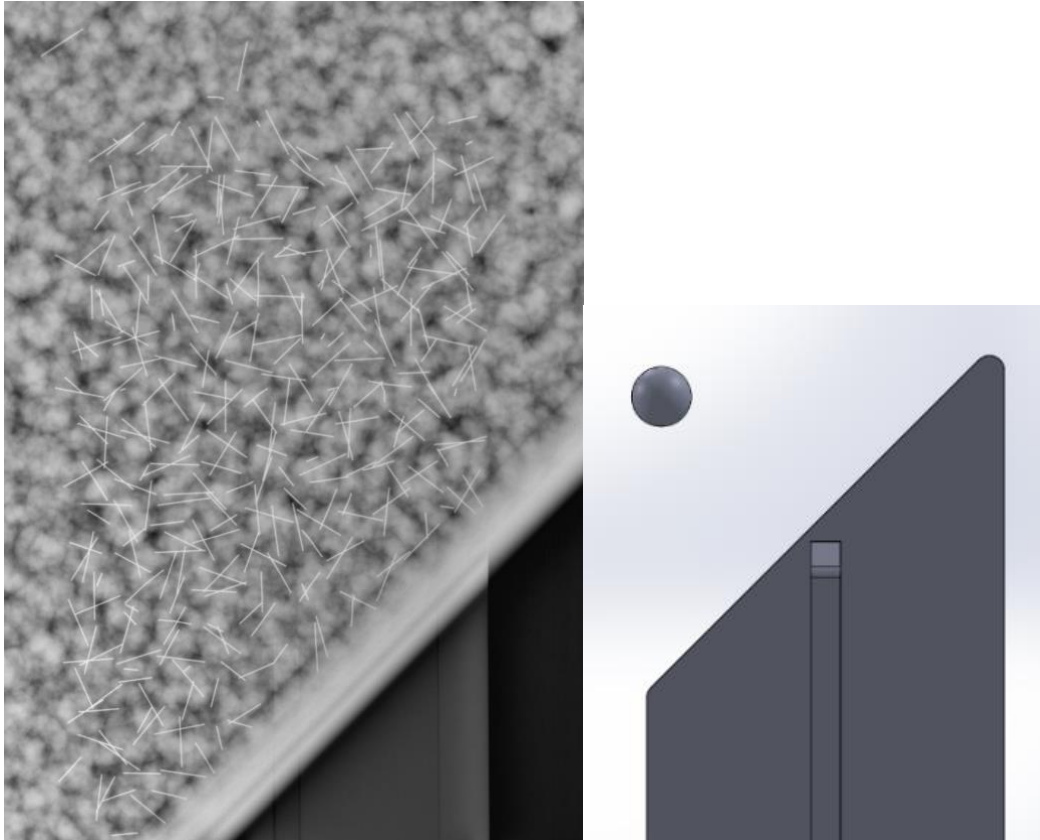


Figure 3-8. Left: x-ray image showing the XZ the plane corresponding to Figure 3-9. Instrumented pebbles can be seen by the tungsten wire running through their centers. In this image, gravity points downward and the blade is inserted upward. Right: corresponding blade orientation and pebble for scale.

A custom CoBIE post processing module was developed to complement X-PETS for this particular experiment. X-PETS is used to track pebbles as they are displaced by the blade insertion. The CoBIE post processing module renders the instrumented pebbles with color and transparency corresponding to individual pebble displacement. The leading edge of the blade is rendered as a white line superimposed on the rendered pebble bed. The location of the blade is known from the actuator control software. An example of the CoBIE post processing module can be seen in Figure 3-9.

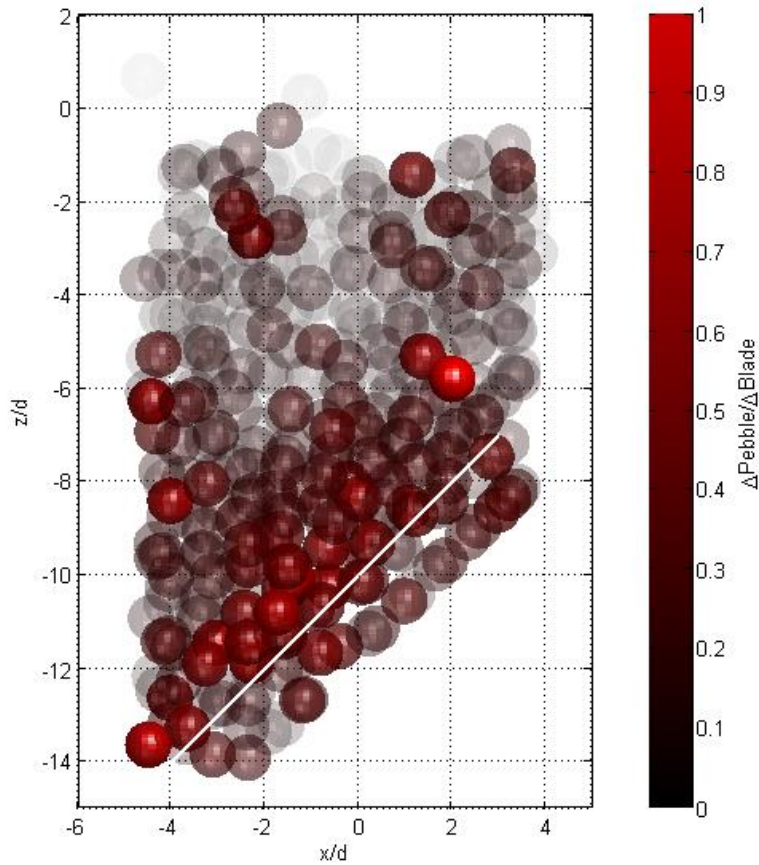


Figure 3-9. Pebble tomography results corresponding to Figure 3-8, showing the XZ plane (gravity points in the $-z$ direction and the blade is inserted in the $+z$ direction $0.98d$). Pebbles are rendered in their final position with varying color and transparency correlated to their normalized centroid displacement from their initial position before the blade was moved. The superimposed white line shows the approximate leading-edge of the final blade position. Pebble centroid displacements are normalized by the blade displacement. Note: $z/d=0$ in this plot does not correspond to $z/d=0$ in the insertion force profile plots.

4 CoBIE Experimental Results

CoBIE tests have returned detailed insertion forces and pebble tomography results, as a function of the blade insertion depth, for many CoBIE testing configurations. These results are summarized in the following sections. Insertion forces are normalized by mg (gravity multiplied by one pebble mass, one non-instrumented pebble weighs almost exactly 1 gram), and lengths are normalized by d (one pebble diameter, 1.257 cm).

4.1 Blade Insertion Hysteresis and Resistance Modes to Blade Insertion

An interesting phenomenon observed by CoBIE is the insertion force profile hysteresis. There is a dramatic difference between the shape of the insertion force profile for a blade inserted into a randomly packed bed, and the insertion force profile of the same blade during a subsequent insertion without any intermediate mixing or reordering of the pebble bed.

4.1.1 Insertion Force Hysteresis

Control blade insertion hysteresis was observed by inserting the 45-degree two-angle no-bullnose control blade into a packed pebble bed with the 45-degree wedge and a pebble bed height of $48d$. For this experiment, retraction forces were also measured by rearranging the force sensors on the blade cradle. Figure 4-1 shows this hysteresis of the insertion forces, as well as the forces required to retract the blade from the pebble bed.

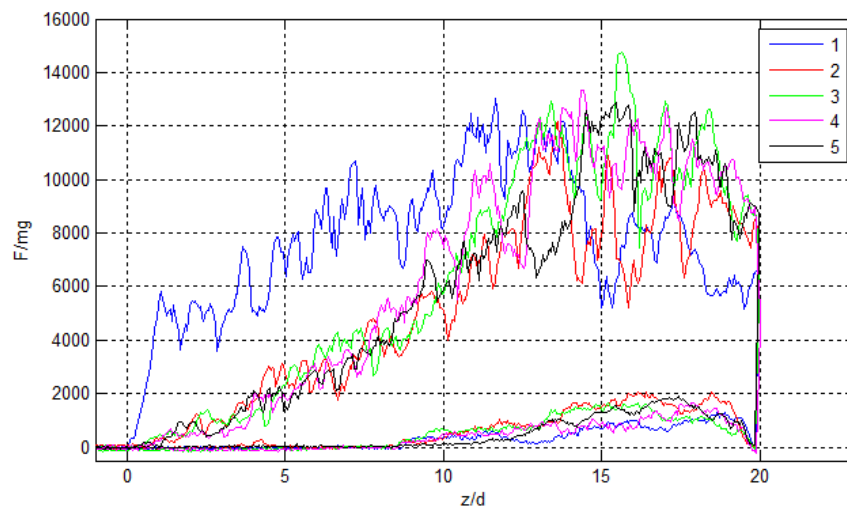


Figure 4-1. Insertion and retraction force hysteresis for five insertions/retractions without intermediate bed mixing. Tests performed using the 45 degree wedge, a pebble bed height of $48d$, and the 45 degree two-angle no-bullnose blade.

The hysteresis in blade insertion forces can be seen to affect the shape of the force profile in Figure 4-1. At a blade insertion of approximately $15d$, the insertion forces for all five tests appear to converge. Figure 4-2 shows that the maximum forces of all tests are nearly constant.

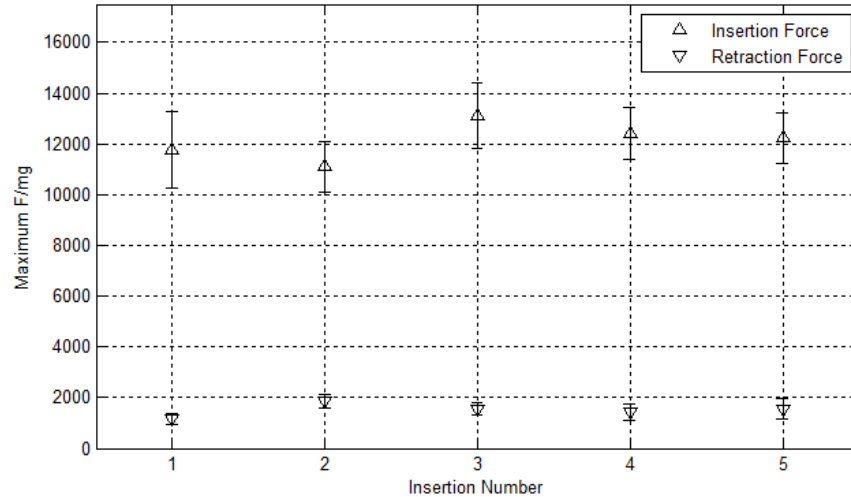


Figure 4-2. Maximum insertion and retraction forces for five subsequent blade insertion/retraction force tests without intermediate bed mixing. Tests performed using the 45-degree wedge, a pebble bed height of $48d$, and the 45-degree two-angle no-bullnose blade.

This data indicates a significant reordering of the pebble bed due to a blade insertion. It is hypothesized that the initial randomly packed pebble bed would have many pebbles directly over the center of the blade, resulting in a sharp immediate increase in force as the blade contacts the pebble bed. It is thought that as the blade is retracted from a fully inserted position, pebbles on either side of it would bridge over the blade center. The reorganized pebble bed would have stress chains much easier to break by the control blade, providing less resistance to motion.

4.1.2 Pebble Location Hysteresis

X-PETS allows the capability to examine and evaluate this hypothesis. The blade used in the following tomography test data is the 45-degree 3-angle full bullnose blade. The left image in Figure 4-3 shows a randomly packed pebble bed before a blade insertion. The middle image in Figure 4-3 shows the same bed after the blade has been fully inserted, and the right image shows the bed after the blade is retracted. The red +’s in Figure 4-3 show the data of interest: the locations of the pebble centroids. In order for the experimental data to support the aforementioned hypothesis, there must be a significant reordering of pebble centroids from the center of the blade before blade insertion, to either side of the blade after blade insertion/retraction.

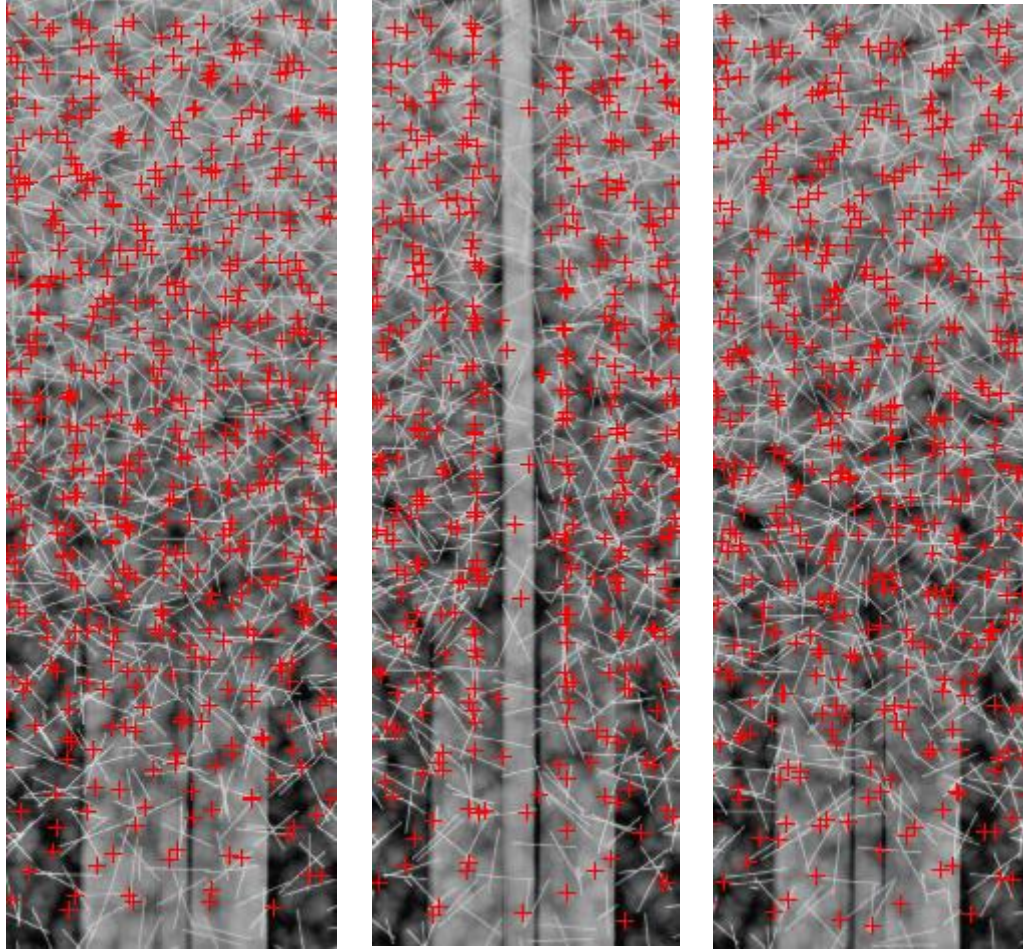


Figure 4-3. X-ray images showing the YZ plane with red +'s indicating the centroids of the instrumented pebbles. Gravity points in the $-z$ direction (towards the bottom of the image) and the blade is inserted in the $+z$ direction (towards the top of the image). Left: randomly ordered bed before blade insertion. Middle: bed shown with blade fully inserted. Right: the same bed after full blade insertion and subsequent retraction.

Figure 4-4, Figure 4-5 and Figure 4-6 show histograms of pebble centroid locations (corresponding to Figure 4-3) relative to the center of the blade before insertion, after insertion, and after retraction, respectively. Figure 4-4 appears to be a near random packing with no discernible pattern and a fair concentration of pebble centroids over the center of the blade ($y/d=0$). Figure 4-5 shows the dramatic shift in pebble locations away from the blade center, as the blade is fully inserted. Figure 4-6 shows the final resting place of the pebbles after the blade is inserted and retracted.

There appears to be a decrease of pebble centroids close to the center of the blade. This supports the hypothesis that the blade insertion significantly reordered the pebble bed to have a lower concentration of pebble centroids at the center of the blade.

To fully demonstrate this effect, the actual reordering of the individual stress chains above the control blade would have to be fully resolved. This is not possible with the X-PETS code, as the

forces on individual pebbles cannot be measured. The histogram in Figure 4-6, given the limitations, still supports the hypothesis.

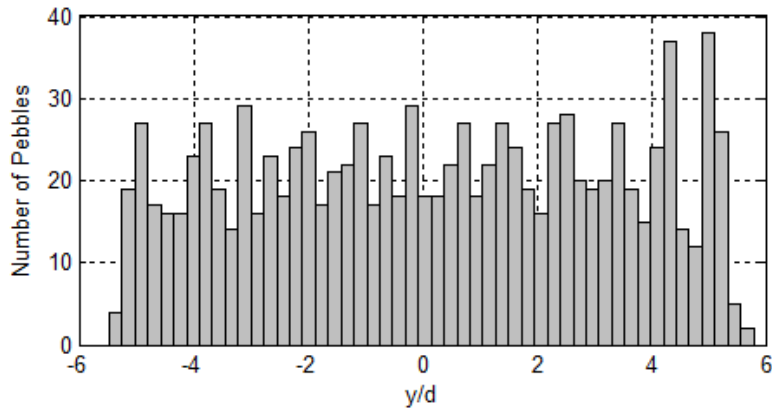


Figure 4-4. Histogram showing the number of pebbles as a function of their centroid y -position before blade insertion (the left image in Figure 4-3). $y/d=0$ corresponds to the center of the blade in the images in Figure 4-3.

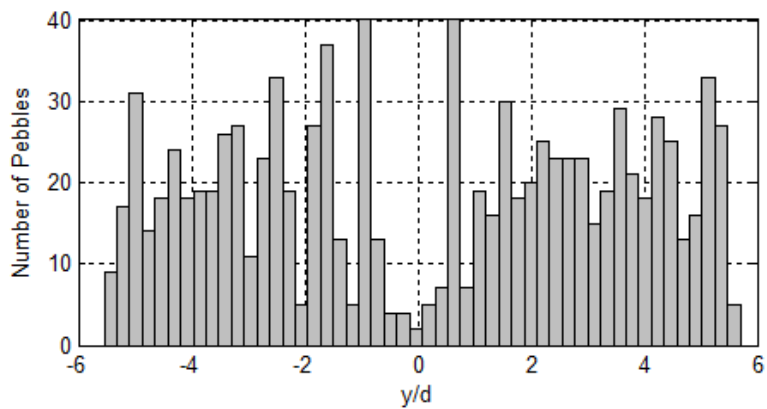


Figure 4-5. Histogram showing the number of pebbles as a function of their centroid y -position while blade is inserted (the middle image in Figure 4-3). $y/d=0$ corresponds to the center of the blade in the images in Figure 4-3.

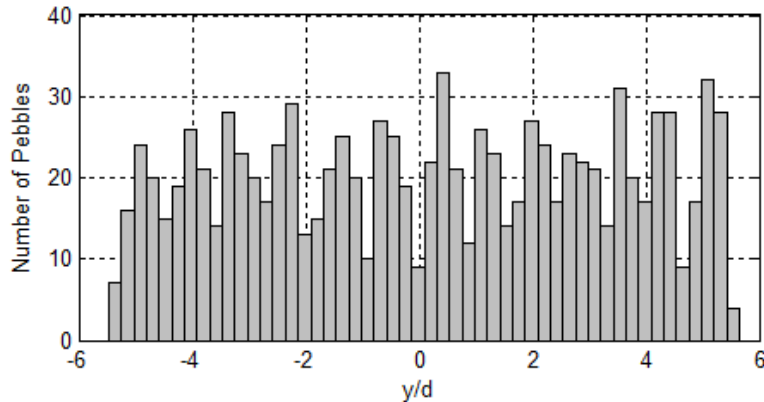


Figure 4-6. Histogram showing the number of pebbles as a function of their centroid y -position after blade retraction (the right image in Figure 4-3). $y/d=0$ corresponds to the center of the blade in the images in Figure 4-3.

4.1.3 Blade Tip Jamming vs. Drag Force

As a blade is pushed through a granular media, it experiences two major forces. The first force is created by the kinetic jamming of pebbles at the tip of the blade. This force is imparted to the tip of the blade by the stress chains in the granular media. The second force is a frictional force on the blade created by the lateral hydrostatic bed pressure that the pebble bed exerts on the flat surface of the blade.

An understanding of these two forces and how they differ is crucial to the design process of control blades. To the author's knowledge, a separate measurement of each force for a geometry similar to the CoBIE control blade has not been previously reported in the literature.

The aforementioned hysteresis study can be interpreted as a separate measurement of these two forces. The insertion force of a blade measures both the kinetic jamming forces exerted on the tip of the blade, as well as the frictional resistance to motion exerted on the sides of the blade. The retraction force of the blade measures only the frictional resistance to motion. The measurements of insertion and retraction forces seen in Figure 4-1 and Figure 4-2 show that the tip jamming force dominates the resistance to insertion.

Consequently, the insertion force should be highly dependent upon blade tip geometry. The following sections will detail the maximum insertion forces of a variety of blade tips. The results help indicate ideal blade tip geometries for use in a PB-FHR reactivity control system.

4.2 The Effect of a Bullnose Tip on Blade Insertion

The roundness of a blade tip is expected to have a significant impact on the blade insertion force as well as the contact force on individual pebbles. A sharp edged blade tip will impart a high local stress where its corners contact pebbles, while a rounded tip will result in a lower local stress contact. It is also predicted that a fully rounded tip will more readily shed pebbles laterally

rather than forcing them upwards against the weight of the bed. This effect can be described by previously studied granular drag effects on discrete shapes [8]. The CoBIE experiment has tested blades with zero bullnose (sharp, 90-degree corners), half bullnose, and full bullnose (fully rounded corners).

Figure 4-7 shows that the roundness of the blade tip does indeed have a significant effect on the maximum insertion force. For the 45-degree two-angle blade, a full bullnose was observed to decrease the maximum insertion force by almost 35%. This dramatic decrease in maximum insertion force highlights the importance of optimized blade design.

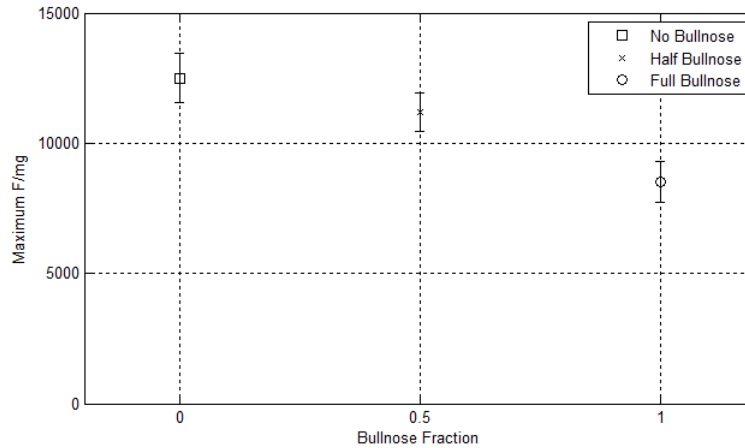


Figure 4-7. Maximum insertion forces +/- one standard deviation vs. blade insertion position for three blades. Test performed with the 45° wedge insert and the 45° two-angle blade with variable bullnose.

It should be noted that this significant decrease in maximum insertion force was not observed between all of the bullnose/non-bullnose blade comparisons. Some blades exhibited negligible decrease in maximum insertion force between the bullnose and non-bullnose variants.

4.3 Effects of Blade Angle and Tip Design

The maximum insertion forces for all blades studied by the CoBIE experiment can be seen in Figure 4-8 and Figure 4-9. The blade with the lowest maximum insertion force was found to be the 45-degree 2-angle full bullnose blade. For both the 2 and 3-angle blade variants, the 45 degree blade tip appears to be the tip angle that results in the lowest maximum insertion force. The exception is the 45-degree 2-angle non-bullnose blade which is observed to have a very large maximum insertion force. This exception was verified as an accurate measurement by repeated testing.

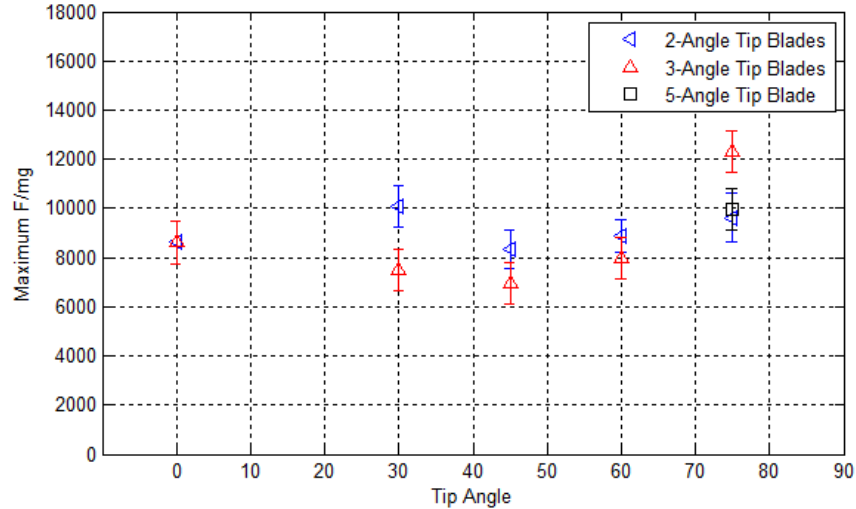


Figure 4-8. Maximum insertion forces for all full-bullnose blades studied.

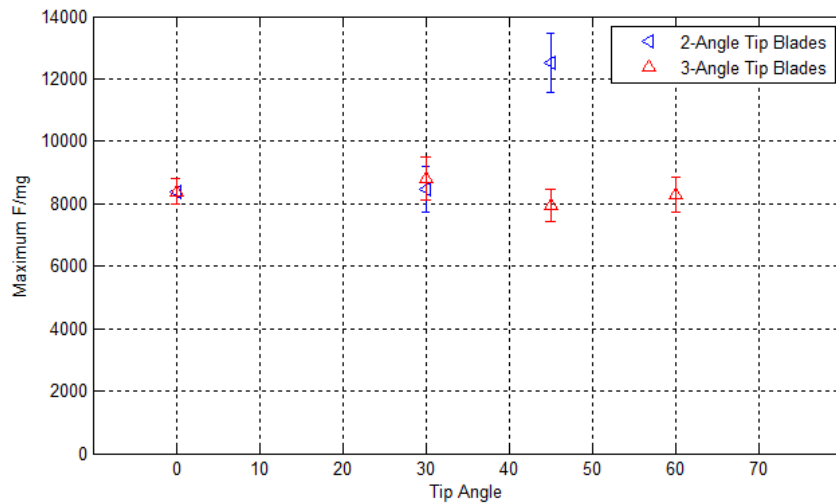


Figure 4-9. Maximum insertion forces for all non-bullnose blades studied.

Another notable result shown in the above figures is the large maximum insertion force measured for the 75-degree blades and the 5-angle blade variant. It is hypothesized that these blades require such large insertion forces because their longer leading edges are in contact with more stress chains in the pebble bed at any given moment.

Tomography tests were conducted to observe how the 45-degree 2 and 3-angle full bullnose blades and the 75 degree 2-angle blade full bullnose blade affected the pebble bed. The digital renders of each tomography test can be seen in Figure 4-10, with pebble color and transparency mapped to respective displacements. The final blade position is shown outlined in green. Each render was generated from five timesteps (blade positions) yielding a total blade displacement of 1 pebble diameter. The difference in vertical blade position between each timestep is $\frac{1}{4}$ of a pebble diameter. Pebbles are only rendered if tracked for all five timesteps, resulting in a high

confidence in the accuracy of the tracking algorithm. Some pebbles far from the blade in the y -direction were not rendered, in order to better display the significant area surrounding the blade.

A concentration of pebble displacement can be observed around the leading edge of each blade. Some pebbles can also be seen displaced a large amount relatively far from the blade leading edge. This observation can be attributed to one of two hypotheses. The first hypothesis is that the stress chains resisting blade motion traverse a large distance from the blade tip, and the weakest connection in the stress chain (the connection that is broken) can be far from the blade. Based on descriptions of stress chain propagation in the literature, this is a reasonable theory. The second hypothesis is that voids exist in the pebble bed, and during a blade insertion, pebbles far from the blade can fall into voids, undergoing a significant displacement.

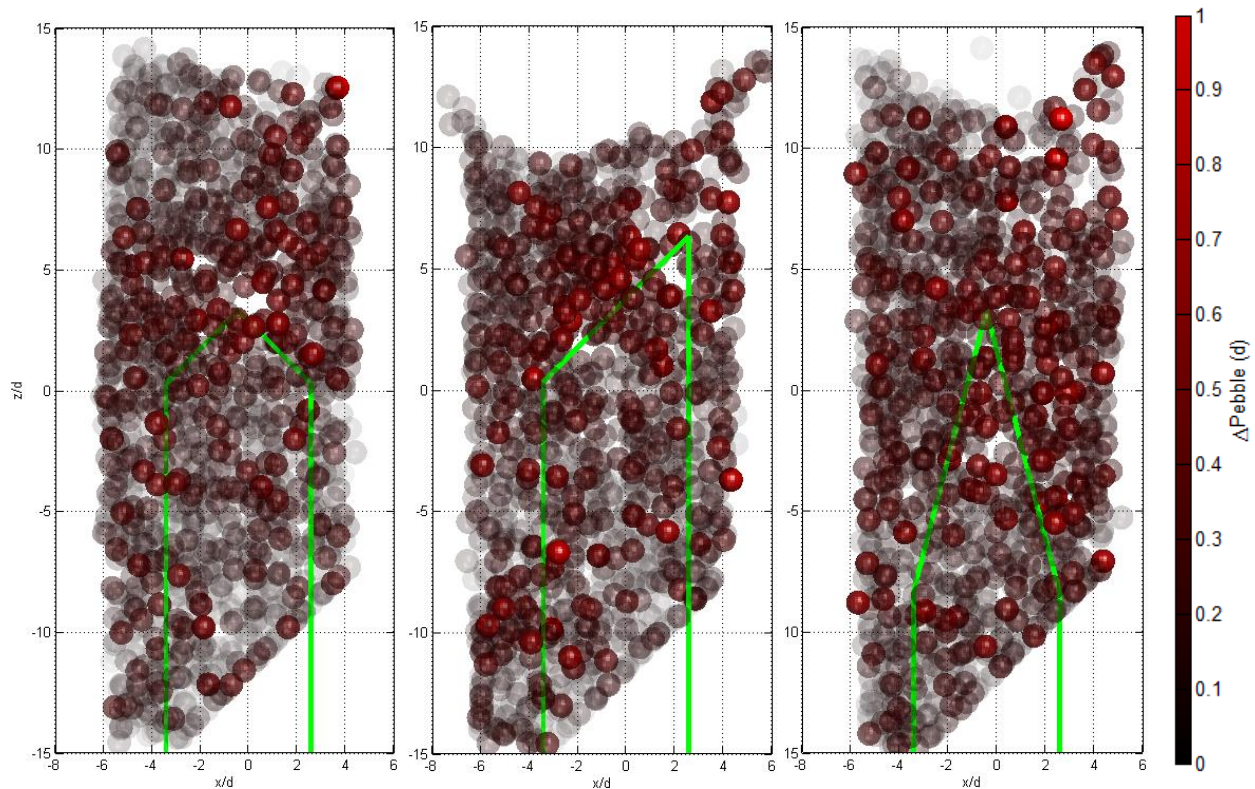


Figure 4-10. Pebble displacement renders using X-PETS R2015b for $\Delta\text{Blade}=1d$ in a square 3100 instrumented pebble channel with side length $10.5d$ in a larger non-instrumented bed of $H=48d$. Pebbles and blade outline (green) shown in their final positions. Left: 45-degree 3-angle full bullnose blade. Middle: 45-degree 2-angle full bullnose blade. Right: 75-degree 3-angle full bullnose blade.

Vector fields provide another method to examine pebble displacement measurements. Figure 4-11 shows the pebble displacement vectors corresponding to the renders seen in Figure 4-10 above. Many of the pebble displacement vectors are observed to be perpendicular to the leading edge of the blade. An explanation for the minimized required insertion forces for the 45-degree blades is that a pebble displacement vector 45-degrees from the horizon is a path of least

resistance, similar to a slip-plane in crystal structures. This could be due to a minimized combination of the resistance of pebble motion due to vertical and horizontal bed pressures exhibited in a pebble bed.

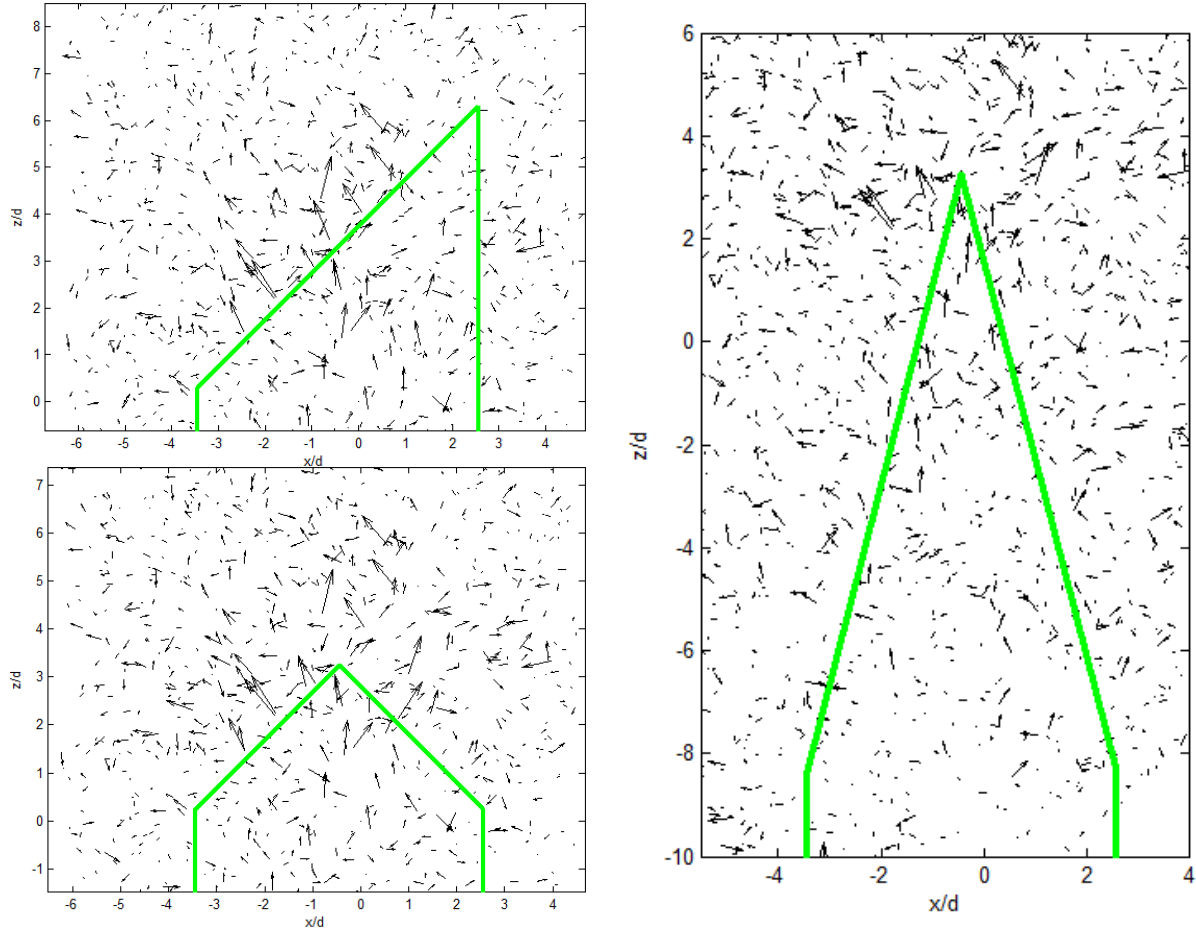


Figure 4-11. Displacement vector fields showing the direction of pebble displacements using X-PETS R2015b for $\Delta\text{Blade}=1d$. Vector magnitudes are exaggerated to show detail.

Pebble displacements can also be treated statistically using a Weibull distribution function to fit an empirical histogram. This result can be seen in Figure 4-11. The distribution function was shown to be nearly identical for the three different tomography tests.

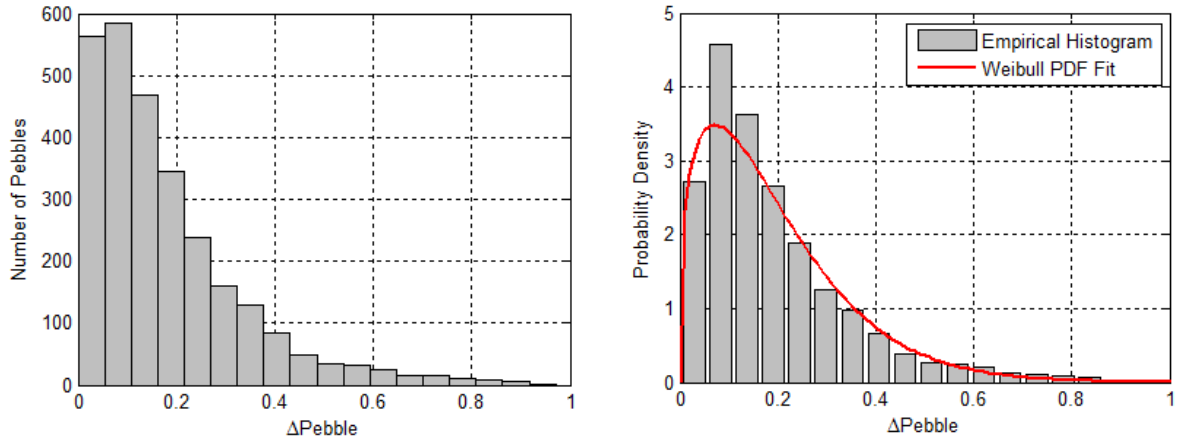


Figure 4-12. Pebble displacements for the 45-degree 2-angle full bullnose blade represented as a histogram (left) and a probability density function (right). Generated using X-PETS R2015b for $\Delta\text{Blade}=1d$. Note the different binning configurations, the binning for the Weibull distribution plot is generated automatically by the distribution fitting algorithm.

5 Discussion of CoBIE Results

5.1 Analysis of Potential Pebble Failure Caused By Control Blade Insertion

Insertion forces for the blade with the least maximum insertion force are shown by the Weibull distribution function in Figure 5-1. The insertion forces are dimensionalized by a single Mk1 PB-FHR pebble body force, buoyant in 650°C flibe, as calculated in section 2.2.

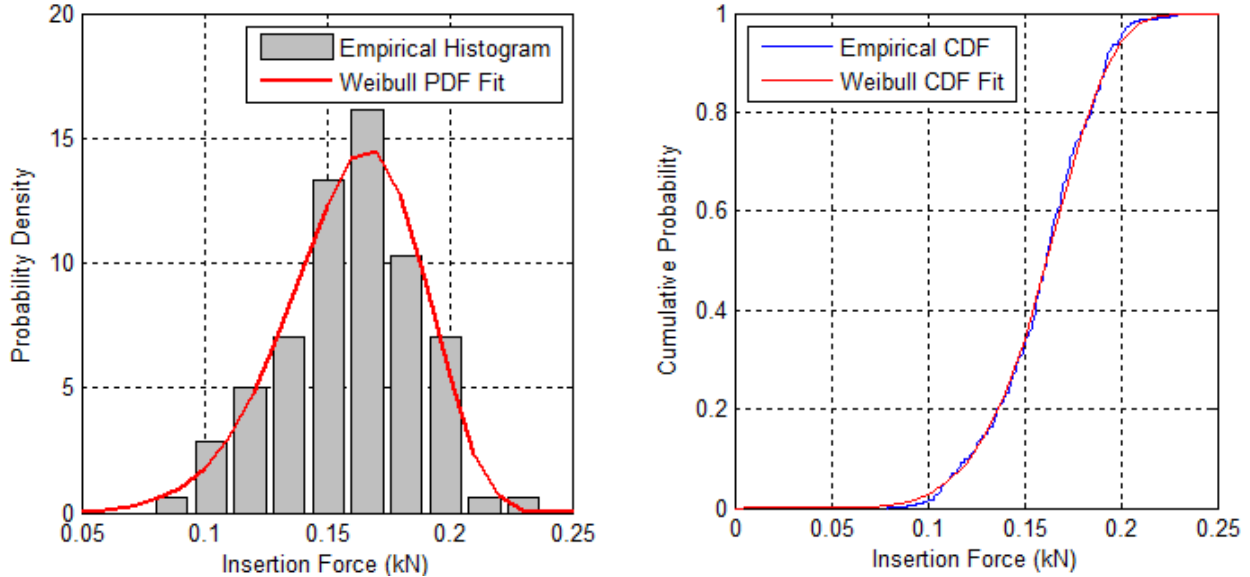


Figure 5-1. Insertion force probability density function (left) and cumulative distribution function (right) for the 45-degree 3-angle full-bullnose blade being inserted into a pebble bed with height $48d$. Forces are scaled for a buoyant Mk1 PB-FHR pebble body force=0.0302N.

Comparing the insertion force distribution to the calculated maximum compressive load limits seen in Table 5-1, it is shown that a single pebble could be loaded with the maximum insertion force measured by CoBIE, and still remain greatly under the compressive load limits. .

Table 5-1. Best-estimate maximum diametrically compressive load limits calculated for a single 3.0-cm fuel pebble [21].

Loading Scenario	Maximum Allowable Applied Force (kN) on a 3.0cm Mk1 PB-FHR Fuel Pebble Based on Maximum Internal Tensile Stress
Steel Plate on Pebble (Crushing Test)	5.9 ± 0.3
Pebble on Pebble	5.6 ± 0.3

Steel Control Blade on Pebble	1.19 ± 0.06
-------------------------------	-------------

Examining the displacement distributions in Figure 4-10, these results indicate a large safety margin for fuel mechanical integrity. The large leading edge of the control blade is observed to displace many pebbles. The maximum compressive force on a single pebble is therefore highly unlikely to result in fracture.

The limits set forth in Table 5-1 also include the conservative assumption that a pebble is under a diametrical loading conditions. That is to say that it is assumed a pebble is compressed by two loading surfaces on opposite sides of its diameter. Multiple loading conditions, as would be the case in a pebble bed, are not considered.

One consideration to increase the likelihood of an even force distribution is to maintain a blade tip angle parallel to the bed interface plane. That is to say if the central reflector that contains the control blade channel has a 45-degree interface plane with the pebble bed, the blade should have a tip that matches this angle. This would ensure that the initial contact force between the blade and the pebble bed is evenly distributed.

5.2 Control Blade Buckling and Deflection Considerations

An additional point of concern is that a control blade either on initial contact with the pebble bed, or once inserted into the pebble bed, could undergo buckling or lateral deflection. A control blade buckling on contact with a pebble bed has the potential to be particularly problematic, as the blade could fail to insert.

The control blade is in essence a column that could buckle given the appropriate axial loading condition, or could undergo cantilever deflection given an appropriate lateral load. Both of these cases are explored in this section using classical column and beam theory.

5.2.1 Blade Loading in the Axial Direction

The general Euler equation for buckling of columns undergoing an axial loading condition is defined as follows [22]:

$$P_{crit} = \frac{\pi^2 EI}{L_e^2} \quad (5.1)$$

With variables defined as follows:

- P_{crit} [N] is the critical axial load on a column at which buckling will occur
- E [Pa] is the elastic modulus of the column
- I [m⁴] is the second (area) moment of inertia of the column's cross section
- L_e [m] is the effective length of the column (Figure 5-2)

The effective length of the column, L_e , in Equation (5.1) is defined for specific loading scenarios as seen in Figure 5-2 [22]:

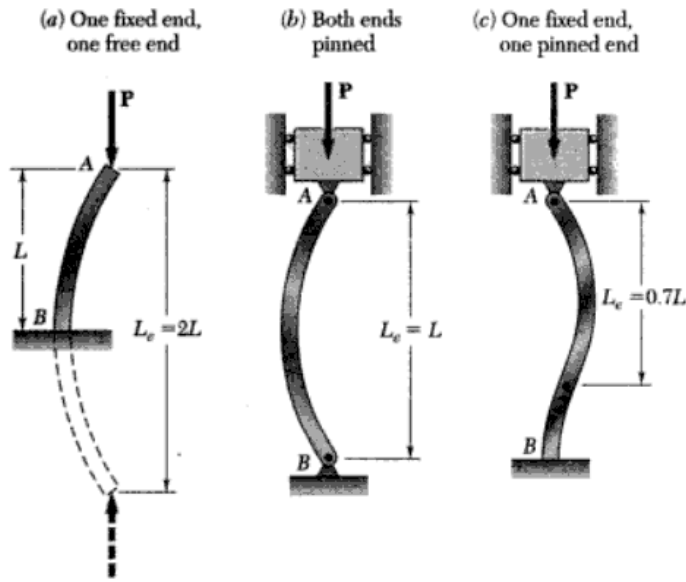


Figure 5-2. Effective lengths of columns with various boundary conditions [22].

All three scenarios in Figure 5-2 are considered for the control blade buckling analysis. The critical load to buckle for each scenario is calculated as a function of unconstrained blade length. The maximum unconstrained blade length is taken to be the approximate height of the Mk1 PB-FHR core, as calculated below from Figure 5-3 (approximately 3 meters). The second (area) moment of inertia is calculated using CAD software (Solidworks) to model the Mk1 PB-FHR control blade (Figure 5-4).

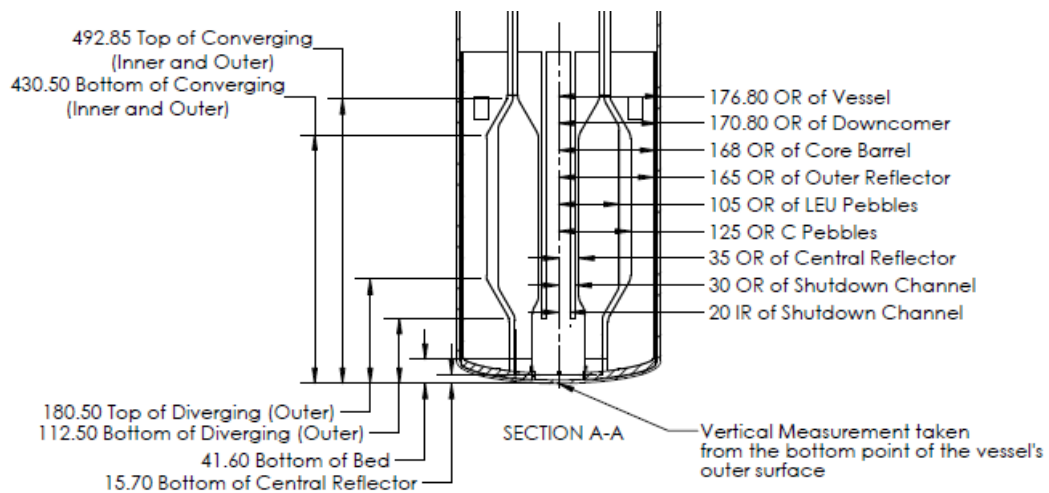


Figure 5-3. Mk1 PB-FHR core dimensions [1]. Units in centimeters.

The maximum unconstrained blade length is taken to be equal to the approximate core height, calculated as follows based on the elevations in Figure 5-3:

$$H_{eff,core} = (Top\ Converging) - (Bottom\ Diverging) - (Height\ of\ Converging\ Region)$$

$$H_{eff,core} = (492.85) - (112.50) - (492.85 - 430.50) = 318\ cm$$

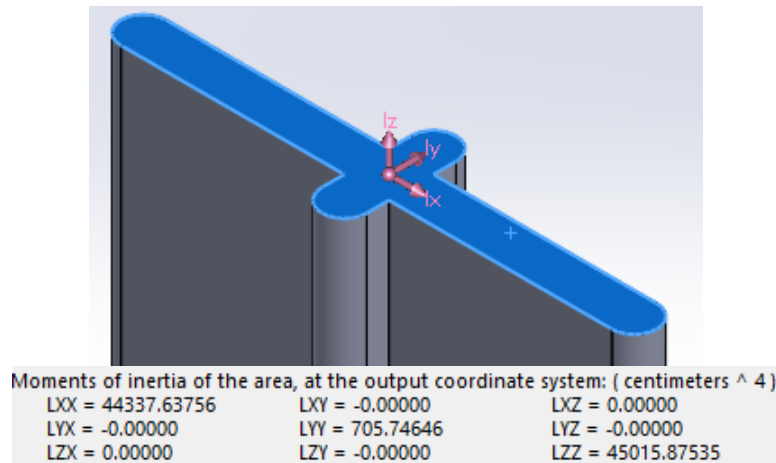


Figure 5-4. Solidworks model of the Mk1 PB-FHR control blade cross section and corresponding second (area) moments of inertia. X and Z moments are based on an arbitrary blade length.

A simplification utilized in this analysis is to assume that the blade is made of homogeneous 316 stainless steel. 316 stainless steel is chosen based on previous discussions of potential control element cladding materials in HTRs [17] and potential structural materials for FHRs [18]. In the actual system, the blade will likely be made of a Boron composite (such as Boron carbide) clad with steel. The resulting input parameters to equation (5.1) can be seen summarized in Table 5-2:

Table 5-2. Summary of relevant parameters for control blade buckling and deflection.

Elastic Modulus of Isotropic 316 SS [19][20]	193 GPa
Second Moment of Inertia of Mk-1 PB-FHR Control Blade	705.75 cm ⁴
Effective Mk1 PB-FHR Core Height	318 cm

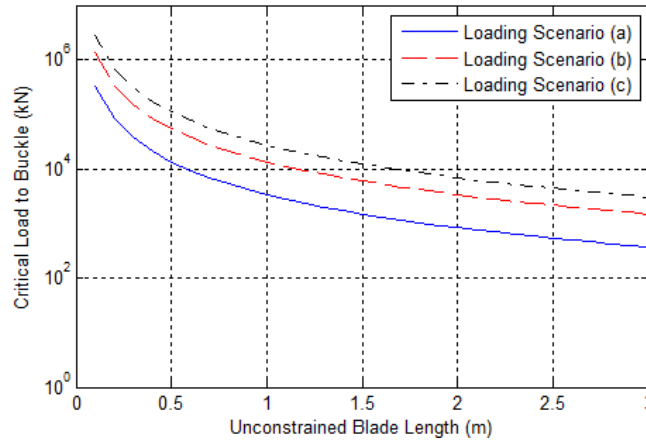


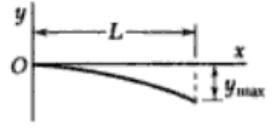
Figure 5-5. Critical axial loads required for buckling as a function of unconstrained blade length for the three loading scenarios seen in Figure 5-2.

The resulting critical axial loads required for buckling seen above in Figure 5-5 are three orders of magnitude greater than the scaled insertion forces measured by the CoBIE tests (Figure 5-1). Therefore, even with the maximum unconstrained blade length of 3 meters in loading condition (c), there will be large safety margins for the control blade buckling on contact with the pebble bed. The critical load to buckle will change for a real control blade with a boron-based core, but it is unlikely that control blade buckling will be a major design concern.

5.2.2 Blade Deflection Due to Lateral Forces

The two blade deflection scenarios due to an uneven lateral load and their corresponding governing equations can be seen below in Table 5-3. Input parameters are the same as in the above buckling case, shown summarized in Table 5-2.

Table 5-3. Deflection of beams in loading conditions relevant to control blade insertion [22].

Loading Condition	Elastic Beam Curve	Maximum Deflection	Elastic Beam Curve Equation
		$y_{\max} = -\frac{PL^3}{3EI} \quad (5.2)$	$y = \frac{P}{6EI}(x^3 - 3Lx^2) \quad (5.3)$
		$y_{\max} = -\frac{wL^4}{8EI} \quad (5.4)$	$y = -\frac{w}{24EI}(x^4 - 4Lx^3 + 6L^2x^2) \quad (5.5)$

With variables defined as follows:

- P [N] is the applied load on a column tip
- E [Pa] is the elastic modulus of the column
- I [m⁴] is the second (area) moment of inertia of the column's cross section
- L [m] is the length of the column being deflected

- w [N/m] is the load distributed over length L
- x and y [m] are Cartesian coordinate system variables defined from the fixed location on the beam

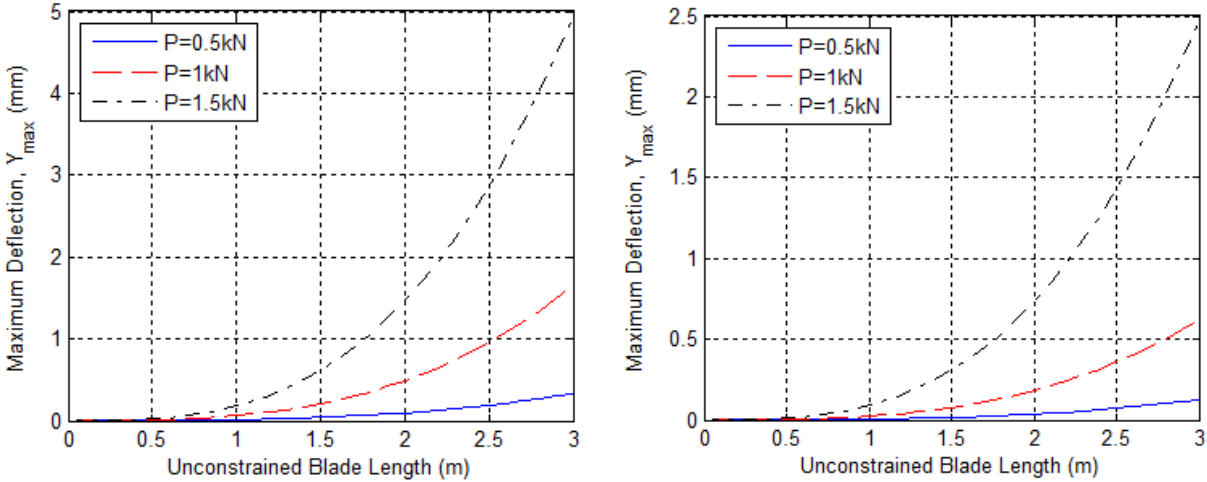


Figure 5-6. Maximum blade deflection at the tip as a function of unconstrained blade length for three different loads. Left: uneven tip loading, equation (5.2). Right: uneven distributed loading, equation (5.4).

The resulting maximum blade deflections are on the order of a fraction of a centimeter over the span of the entire 3 meter unconstrained control blade. Furthermore, this maximum deflection would be the result of the maximum insertion force measured by CoBIE (Figure 5-1) loaded entirely on one side of the blade. It is a far more likely case that only a small fraction of this insertion force would be loaded in a lateral and uneven manner on the blade, resulting in a negligible deflection at the blade tip. It is unlikely, based on these results, that blade deflection due to uneven tip loading will prove to be a major design concern.

5.3 Scaling Distortions Analysis

5.3.1 Effects of the CoBIE Test Silo Constraints

The distortions created by the limited size of the CoBIE pebble bed silo must be considered. Both the silo area and height have the ability to provide distortions. Narrow containers such as CoBIE can exhibit significant effects from the walls, while the limited bed height of CoBIE is not fully representative of a full-scale Mk1 PB-FHR core.

In a narrow container such as the CoBIE test silo, the walls have the potential to carry a large amount of the vertical bed load due to friction. This phenomena has been shown by DEM simulations to result in asymptotic behavior in vertical bed pressure [16]. During blade insertion into the CoBIE test silo, this phenomena would result in insertion forces reaching an asymptote as the bed height increased. Figure 5-7 shows the insertion force profiles for a blade being

inserted into a pebble bed of five incremental heights. The maximum bed height achievable in the CoBIE test silo is $48d$ (48 pebble diameters). Figure 5-8 shows that the maximum insertion force increases approximately linearly with pebble bed height. This shows that up to the maximum CoBIE bed height, the container walls do not support a significant portion of the vertical load. The slope of the curve in Figure 5-8 likely changes as H/d approaches the lower limit because the tip of the blade approaches the top free surface of the pebble bed at this extreme.

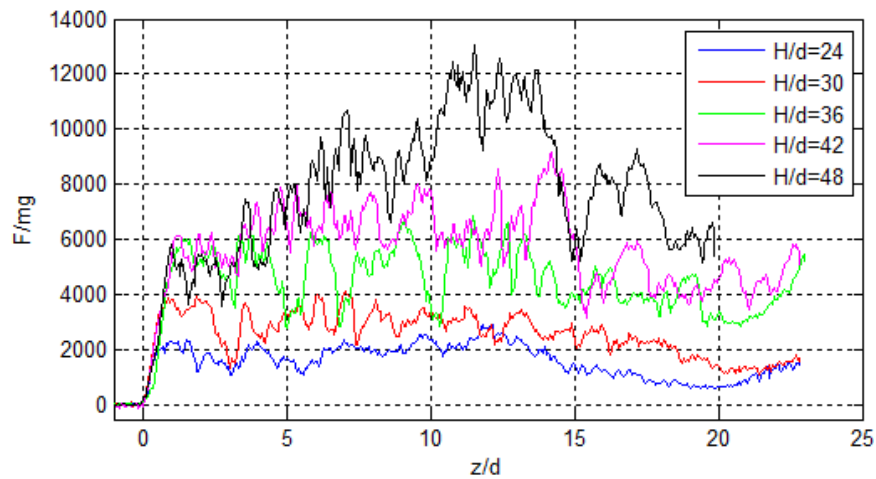


Figure 5-7. Insertion forces vs. blade insertion position ($z/d=0$ is where the blade initially contacts the pebble bed) for five pebble bed heights. Test performed with the 45° wedge insert and the 45° two-angle no-bullnose blade.

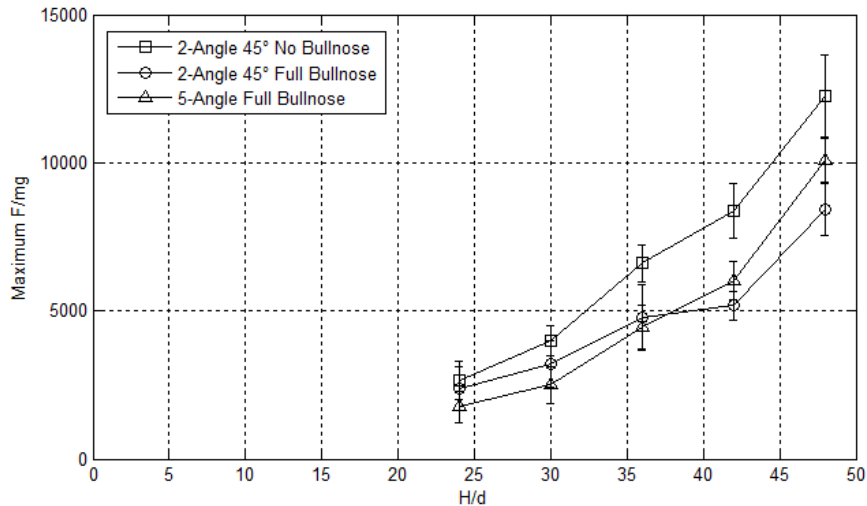


Figure 5-8. Maximum insertion forces with one-sigma uncertainty vs. pebble bed height.

It must also be taken into consideration that the maximum bed height of $48d$ is approximately half of the bed height in the Mk1 PB-FHR design [1]. Assuming no asymptotic loading behavior in the Mk1 design, the actual control blade insertion forces could be twice as large as the forces

observed by CoBIE. Based on the insertion force profile seen in Figure 5-1 and the maximum load limits in Table 5-1, the maximum insertion forces for a bed fully scaled to the Mk1 PB-FHR height should still be well below the load limits in Table 5-1.

5.3.2 Velocity Distortions

During a reactor shutdown event in a typical light water reactor, control rods are inserted very rapidly. In a pebble bed direct reactivity insertion event, a major concern is that a very fast blade insertion velocity would cause a much greater amount of force to be imparted to pebbles, possibly increasing the fracture probability.

CoBIE has the capability to test a limited range of control blade insertion velocities. The maximum and minimum insertion velocities are constrained by the maximum and minimum operating speeds of the linear actuator system. Because the X-PREX facility was designed to study slow dense granular flow, the linear actuator was not designed for high-speed actuation. Figure 5-9 shows the range of insertion velocities tested by CoBIE.

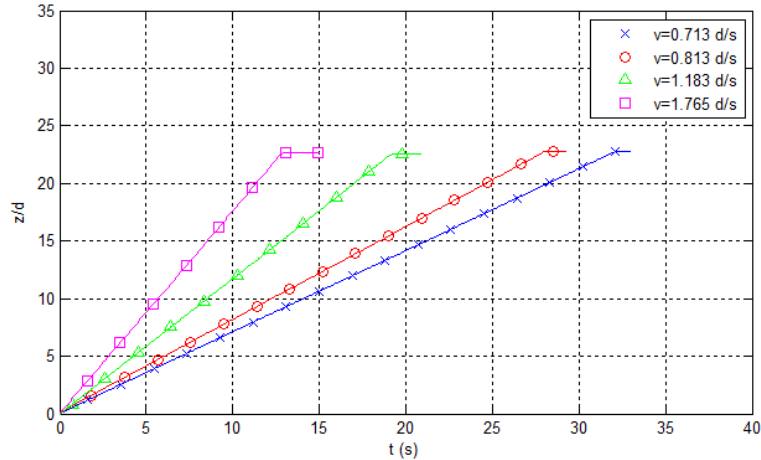


Figure 5-9. Insertion profiles for four insertion velocities. Velocities are measured in pebble diameters per second.

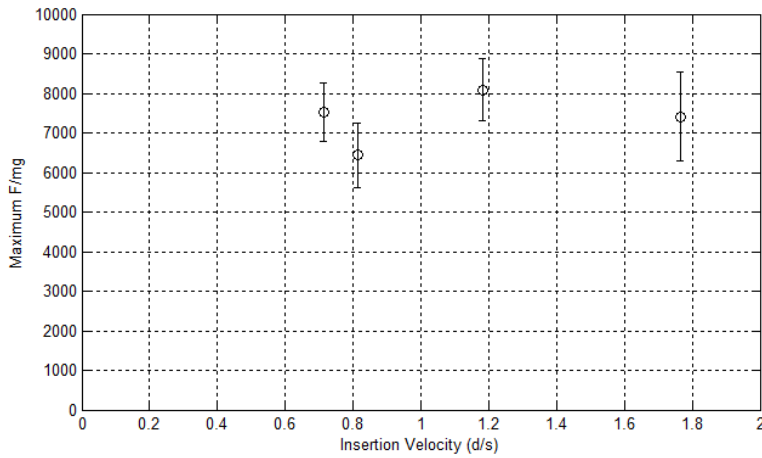


Figure 5-10. Maximum insertion force for four insertion velocities. Tests performed using the 45-degree wedge, a pebble bed height of $48d$ and the 45-degree 2-angle full-bullnose blade.

Figure 5-10 shows no correlation between velocity and insertion force, over the tested velocity range. This non-correlation can be explained by a low-velocity regime, previously described in the literature [10]. Drag force on an object is found to be a strong function of velocity only when the object’s velocity is great enough to “fluidize” the grains in a packed bed. Drag forces below the bed fluidization threshold are considered to be in a “low-velocity regime”, and are not dependent upon velocity. The velocity threshold for the fluidization of a bed is seen defined here [10]:

$$v_{threshold} = \frac{\sqrt{2gd_g}}{10} \quad (5.6)$$

Where:

- $v_{threshold}$ [m/s] is the threshold velocity over which the bed is fluidized and drag force becomes a function of velocity
- g [m²/s] is the acceleration due to gravity
- d_g [m] is the grain (or pebble) diameter

Equation (5.6) can also be used to calculate the velocity threshold in units of pebble diameters per second (units used in Figure 5-9 and Figure 5-10) as follows:

$$\frac{v_{threshold}}{d_g} = \frac{1}{10} \sqrt{\frac{2g}{d_g}} \quad (5.7)$$

For CoBIE, the velocity threshold is calculated to be approximately 4 d/s, which as expected, is greater than the upper limit of the actuator velocity.

If the control blade insertion velocity in the Mk1 PB-FHR system is specified to be faster than the velocity threshold calculated using equation (5.6), additional measurements taken in the fast velocity regime must be performed to ensure sufficiently low forces are imparted to the fuel pebbles.

5.3.3 Effects of Lubricity, Coefficient of Restitution and Coolant Flow

So far, this report has assumed that the surface characteristics are the same between the CoBIE pebbles and the Mk1 PB-FHR pebbles. This section compares previously measured pebble surface characteristics, and discusses the resulting scaling distortions.

The static Coulomb friction coefficient was evaluated for instrumented CoBIE pebbles (polypropylene with tungsten wire inserts) on several plastic surfaces. A simple ramp test was performed, which consisted of a pebble-holder resting on a flat surface (the ramp). The pebble-holder was designed to create an ideal pebble-on-ramp contact for friction characterization. The flat surface was inclined until the pebble-holder started to slide. The critical angle was measured to indicate the static coefficient of friction [4].

Table 5-4. CoBIE/X-PREX pebble surface static friction measurements [5].

Sheet Material	Static Friction Coefficient (μ_c)
Polypropylene (Pebble Material)	0.29
Cast Acrylic (Container Material)	0.39
Polycarbonate (Blade Material)	0.41

The friction coefficients for a graphite-on-graphite contact in molten salt (FLiNaK) were measured at UC Berkeley [13] in 2009, and can be seen in Table 5-5.

Table 5-5. Graphite-on-graphite experimentally measured coefficients of friction in molten salt (FLiNaK) [13].

Temperature (°C)	Normal Mass (kg)	μ_i	μ_s	σ_μ
492	0.915	.237	.273	$\pm .0328$
	1.39	.190	.256	$\pm .0216$
	1.86	.180	.253	$\pm .0161$
525	0.915	.224	.260	$\pm .0328$
	1.39	.189	.253	$\pm .0216$
	1.86	.182	.255	$\pm .0161$
559	0.915	.215	.251	$\pm .0328$
	1.39	.187	.251	$\pm .0216$
	1.86	.177	.250	$\pm .0161$

The static coefficient of friction between fuel spheres lubricated by a molten salt is approximately to be 0.25, while the coefficient of friction between dry plastic spheres is approximately 0.29. Drag and blade insertion forces are therefore expected to be enhanced in the CoBIE tests compared to forces in a PB-FHR, although the distortion is likely minimal.

Another parameter that governs properties in a granular bed is the coefficient of restitution [9]. The coefficient of restitution provides a measure of elastic rebound between a surface and an object. The coefficient can be calculated by the ratio of the kinetic energy of an incoming object and the kinetic energy of the same object after having collided with a surface. The coefficient of restitution can be experimentally measured by dropping a pebble at a certain height, and measuring the height after rebound, based on the relationship between kinetic and gravitational potential energy. The resulting equation is as follows:

$$C_R = \sqrt{\frac{h_2}{h_1}} \quad (5.8)$$

20 drop tests were performed for the instrumented CoBIE pebbles (polypropylene with tungsten wire inserts) from an initial height $h_1 = 57.5 \pm 0.1$ cm onto varying sheet materials. The resulting coefficients of restitution can be seen in Table 5-6.

Table 5-6. CoBIE/X-PREX pebble mechanical contact measurements [5].

Sheet Material	Bounce Height (h_2)	Coefficient of Restitution (C_R)
Polypropylene (Pebble)	35.1 ± 0.8	0.781 ± 0.014
Cast Acrylic	37.5 ± 0.6	0.807 ± 0.009
Acetal Resin	30.9 ± 0.6	0.733 ± 0.012
Polycarbonate	35.9 ± 0.6	0.790 ± 0.011

To the author’s knowledge, the coefficient of restitution of graphite fuel spheres in an actual reactor system is unknown. The scaling distortion due to varying coefficients of restitution is therefore not currently possible to quantify. Table 5-6 is recorded so that future tests may attempt to quantify this distortion.

The effects of coolant flow through the pebble bed during blade insertion were not studied by the CoBIE system. Furthermore, flow effects on granular drag have not been reported previously in the literature, to the knowledge of the author. In the Mk1 PB-FHR design, the coolant flow path is directed upwards, in the same direction as the buoyant force. It is anticipated that the coolant pressure drop across the core will be directly related to an increased hydrostatic bed loading force, and therefore an increased blade insertion force. This effect is currently not quantified.

6 Conclusions and Recommendations for Future Work

The Control Blade Insertion Experiment (CoBIE) successfully measures both the forces required for control blade insertion into a packed pebble bed and the pebble movement in response to such an insertion.

A control blade with a 45-degree 3-angle tip design and fully rounded edges is shown to be the optimal blade design for minimizing blade insertion force. Scaled CoBIE insertion forces for the aforementioned blade design are calculated to be well below the limits for diametrical loading of a 3cm graphite fuel sphere.

A simplified buckling and deflection analysis are performed, and result in significant safety margins for these design cases, based on the CoBIE scaled insertion forces.

It is estimated that for the full core height of the Mk1 PB-FHR, the blade insertion force would still remain below fuel load limits. These results support the use of direct control blade insertion as a viable reactivity control method for PB-FHRs.

The research performed would benefit from: experimental quantification of the effects of scaling distortions, experimental measurements of the external load limits of 3cm PB-FHR graphite fuel sphere, and simulation measurements of the individual contact forces that pebbles are subjected to during a direct blade insertion using DEM software.

References

- [1] C. Andreades, et al., “Technical Description of the ‘Mark 1’ Pebble-Bed Fluoride-Salt-Cooled High-Temperature Reactor (PB-FHR) Power Plant,” Department of Nuclear Engineering, U.C. Berkeley, Report UCBTH-14-002, 2014.
- [2] S. Chang, A Gonzalez, J. Kong, N. Satterlee. “PB-FHR Reserve Shutdown System”. Department of Nuclear Engineering, U.C. Berkeley, Report UCBTH-12-008, 2012.
- [3] S. Rubin. “Briefing on Visit of the NRC Delegation to Germany on Safety Aspects of HTR Technology”. Nuclear Regulatory Commission. August 1, 2001. Document number ML021960035. pbadupws.nrc.gov/docs/ML0219/.
- [4] U. Cleve. “Breeding of Fissile Uranium 233 Using Thorium 232 with Pebble Fuel Elements”. *Attaining Freedom Through Necessity: The Last Chance for Humanity*. Schiller Institute Conference Proceedings. Frankfurt, Germany. April 13-14, 2013.
- [5] M. Laufer, G. Buster, “X-Ray Pebble Recirculation Experiment (X-PREX) Design and Initial Experimental Results” Department of Nuclear Engineering, U.C. Berkeley, Report UCBTH-15-002, 2014.
- [6] D. F. Williams, L. M. Toth, K. T. Clarno. “Assessment of Candidate Molten Salt Coolants for the Advanced High-Temperature Reactor (AHTR)”. Oak Ridge National Lab, Nuclear Science and Technology Division. ORNL/TM-2006/12. March 2006.
- [7] I. Alber, P. Tegzes, B. Kahng, R. Albert, J. G. Sample, M. Pfeifer, A.-L. Barabasi, T. Vicsek, P. Schiffer. “Jamming and Fluctuations in Granular Drag”. *Phys. Rev. Lett.* 84, 5122 – Published 29 May 2000.
- [8] I. Albert, J. Sample, A. Morss, S. Rajagopalan, A.-L. Barabasi, P. Schiffer. “Granular drag on a discrete object: Shape effects on jamming”. *Physical Review E*, Vol. 64, 061303. 7 November 2001.
- [9] R. P. Behringer, D. Howell, L. Kondic, S. Tennakoon, C. Veje. “Predictability and Granular Materials”. *Physica D* Vol. 133 (1999) 1-17.
- [10] R. Alber, M. A. Pfeifer, A.-L. Barabasi, and P. Schiffer. “Slow Drag in a Granular Medium”. *Physical Review Letters* Vol. 82 (1), January 4, 1999.
- [11] C. Tang, Y. Tang, J. Zhu, Y. Zou, J. Li, X. Ni. “Design and Manufacture of the Fuel Element for the 10 MW High Temperature Gas-Cooled Reactor”. *Nuclear Engineering and Design*, Vol. 218 (2008) pg. 91-102.
- [12] M. E. Cates, J. P. Wittmer, J.-P. Bouchaud, P. Claudin. “Jamming and Static Stress Transmission in Granular Media”. *Chaos: An Interdisciplinary Journal of Nonlinear Science*. Vol 9 (3), 511 (1999).
- [13] R. Hong, S. Huber, K. Lee, P. Purcell, S. Margossian, J.-D. Seelig. “Reactor Safety and Mechanical Design for the Annular Pebble-Bed Advanced High Temperature Reactor”. Department of Nuclear Engineering, U.C. Berkeley, Report UCBTH09-001, May 2009.
- [14] R. R. Kinnison, “Applied Extreme Value Statistics”. Macmillan Publishing Company, New York. Copyright 1985 Battelle Memorial Institute. Pg. 17-23.

- [15] K. Rollig, W. Theymann. “Operational Requirements of Spherical HTR Fuel Elements and their Performance”. Hochttemperatur-Reactorbau GmbH. Mannheim, Federal Republic of Germany. IAEA. INIS Vol. 31 Issue 41 Ref. Number: 31049614.
- [16] J. Landry, L. Silbert, S. Plimpton. “Confined granular packings: Structure, stress, and forces”. *Physical Review E*, Vol 67, 041303. 21 April 2003.
- [17] General Atomics. “General Atomic’s Prismatic Modular High Temperature Gas Cooled Reactor”. International Atomic Energy Agency, Advanced Reactors Information System (IAEA, ARIS), Technical Data on Gas Cooled Reactors (GCR).
- [18] G. Zheng, B. Kelleher, G. Cao, M. Anderson, T. Allen, K Sridharan. “Corrosion of 316 Stainless Steel in High Temperature Molten Salt Li_2BeF_4 (FLiBe) Salt”. *Journal of Nuclear Materials* 461, 2015, 143-150.
- [19] North American Stainless. “Flat Product Stainless Steel Grade Sheet 316 (S31600)/EN 1.4401”. ASTM and ASME certified. 2010.
- [20] AK Steel. “Product Data Sheet. 316/316L Stainless Steel UNS S31600 AND UNS S31603”. AK Steel Corporation, West Chester, OH, 2007.
- [21] G. Buster, M. Laufer, P. Peterson. “Fracture Analysis of Reduced Diameter Spherical Graphite Fuel Elements under Diametrical Loading Conditions”. Department of Nuclear Engineering, U.C. Berkeley, Report UCBTH-15-004. May, 2015.
- [22] F. P. Beer, E. R. Johnston Jr., J. T. DeWolf. “Mechanics of Materials (In SI Units)”. Tata McGraw-Hill Education. 3rd Edition. 2004. Pg. 530-662.